nature communications

Article

https://doi.org/10.1038/s41467-025-56346-3

The 40S ribosomal subunit recycling complex modulates mitochondrial dynamics and endoplasmic reticulum - mitochondria tethering at mitochondrial fission/fusion hotspots

Received: 22 April 2024

Accepted: 16 January 2025

Published online: 25 January 2025

Check for updates

Foozhan Tahmasebinia[1], Yinglu Tang[1], Rushi Tang[2], Yi Zhang[1], Will Bonderer[1], Maisa de Oliveira[1], Bretton Laboret[1], Songjie Chen[3], Ruiqi Jian[3], Lihua Jiang[3], Michael Snyder[3], Chun-Hong Chen[4], Yawei Shen[5,6], Qing Liu[5,6], Boxiang Liu[2,7,8,9,10,11] ✉ & Zhihao Wu[1] ✉

The 40S ribosomal subunit recycling pathway is an integral link in the cellular quality control network, occurring after translational errors have been corrected by the ribosome-associated quality control (RQC) machinery. Despite our understanding of its role, the impact of translation quality control on cellular metabolism remains poorly understood. Here, we reveal a conserved role of the 40S ribosomal subunit recycling (USP10-G3BP1) complex in regulating mitochondrial dynamics and function. The complex binds to fission-fusion proteins located at mitochondrial hotspots, regulating the functional assembly of endoplasmic reticulum-mitochondria contact sites (ERMCSs). Furthermore, it alters the activity of mTORC1/2 pathways, suggesting a link between quality control and energy fluctuations. Effective communication is essential for resolving proteostasis-related stresses. Our study illustrates that the USP10-G3BP1 complex acts as a hub that interacts with various pathways to adapt to environmental stimuli promptly. It advances our molecular understanding of RQC regulation and helps explain the pathogenesis of human proteostasis and mitochondrial dysfunction diseases.

Maintaining cellular homeostasis relies on the dynamic integrity of the functional proteome, which necessitates a proper equilibrium between protein synthesis, folding, and degradation[1]. Various mechanisms surveil the quality of proteins. Prior research primarily concentrated on the quality control of mature proteins. As of late, ribosome-associated quality control (RQC) has gained recognition for its importance in evaluating the quality of nascent peptides[2–4]. There has been an increasing emphasis on the correlation between translation quality control mechanisms, such as RQC, and metabolic pathways in addressing the problem of translation stalls. Recent reports indicate that translational arrest leads to translational repression via the EDF1-GIGYF2-EIF4E2 feedback loop[5], and induces stress responses through the ZAKα/p38/JNK[6], GCN2/1/20[7], SAPK (p38/JNK)[8], and cGAS-STING pathways[9]. In addition, ribosome collision elicits ribotoxic stress response and impacts the AMPK/mTORC1 signaling pathway[10].

Protein synthesis is also one of the most energetically demanding processes in cellular metabolism, and adjustments to protein

A full list of affiliations appears at the end of the paper. ✉e-mail: boxiangliu@nus.edu.sg; zhihaowu@smu.edu

translation are inevitably accompanied by swift alterations in energy metabolism[11,12]. Nevertheless, the mechanisms by which cells reshape energy synthesis at its origin upon RQC have yet to be determined. Prior research has revealed that during RQC, stalled nascent peptides of selective nuclear-encoded mitochondrial proteins are elongated by adding C-terminal alanine and threonine tails (CAT-tails). The accumulation of CAT-tailed proteins compromises mitochondrial functions, which is counteracted by Vms1 through catalyzing the cleavage and release of peptidyl-tRNA in 60S subunits[13–16]. This suggests a potential association between RQC and mitochondrial homeostasis. In the interim, a recent study indicated that the loss of function of Hel2, the yeast homolog of ZNF598, results in the mis-localization of secretory proteins into mitochondria, subsequently causing mitochondrial dysfunction[17]. However, these regulations appear to be reactive adaptations to mitochondrial dysfunction rather than proactive adjustments.

RQC includes multiple steps. Upon translational arrest, disomes or trisomes (disomic or trisomic ribosomes) are first sensed by the ZNF598-RACK1 complex by recognizing the 40S-40S interface of collided ribosomes[18–20]. Reversible monoubiquitination is marked by ZNF598 (zinc finger protein 598) on RPS10 (40S ribosomal protein S10), and by RNF10 (RING finger protein 10) on RPS2 and RPS3[21,22]. The ASC-1 complex then disassembles the collided ribosomes, enabling the ABCE1-PELO-HBS1L complex to initiate subsequent processes of the 80S ribosome by splitting it into the 60S (large) and 40S (small) subunits[23–25]. The 60S ribosomal subunit binds to NEMF (nuclear export mediate factor with *Drosophila* ortholog being Clbn) and LTN1 (E3 ubiquitin-protein ligase Listerin with *Drosophila* ortholog being Ltn1), releasing stalled peptides through the CAT-tailing mechanism[26]. Meanwhile, the 40S ribosomal subunit undergoes recycling after deubiquitination by the G3BP1-family-USP10 complex[27]. The biological significance of 40S subunit recycling is not as well understood as that of CAT-tailing and 60S subunit recycling processes[13,28,29].

G3BP1 and USP10 have recently been identified as key components in the 40S ribosomal subunit recycling complex[27]. The family of G3BP1 (Ras GTPase-activating protein-binding protein 1) proteins, which includes G3BP1 and G3BP2 in humans, are highly conserved RNA-binding proteins across species. They are widely expressed in all eukaryotes and are found in both the nucleus and cytoplasm to regulate RNA metabolism[30,31]. G3BP1 family proteins are recognized as representative indicators and core elements of stress granules, which comprise the arrested 48S pre-translational initiation complex induced by cytotoxic stress and other RNA-binding proteins[32]. Overexpression of human G3BP1 family proteins promotes the assembly of stress granules, while loss-of-function impedes the assembly[33–35]. USP10 plays a multifaceted role as a deubiquitinase in various pathways, including but not limited to regulating paraptosis[36], deubiquitinating Yorkie protein in the Hippo pathway[37], stabilizing LC3B in autophagy[38], and facilitating the aggresome formation in apoptosis[39]. The substrates of USP10 exhibit a diverse range of stress modulators, indicating its critical role in regulating programmed cell death. USP10 has also been reported to interact with AMPK (AMP-activated protein kinase) to ensure effective responses to fluctuations in cellular energy status[40]. The interactions between USP10 and G3BP1 family proteins were first described in a global proteomic analysis of deubiquitinates and their associated protein complexes[41,42]. They were later found to control the recycling of the 40S ribosomal subunit[27]. As such, we highly suspect that the USP10-G3BP1 complex can talk to energy metabolic pathways during RQC.

Mitochondria are the primary site for producing adenosine triphosphate (ATP), the cell's energy currency. The morphology and function of mitochondria are closely interconnected with their quality[43]. Alterations in these two mitochondria attributes are correlated with fluctuations in cellular energy metabolism. Recent studies have uncovered a connection between changes in mitochondrial morphology and activity regulation with a specialized structure known as the endoplasmic reticulum (ER) - mitochondria contact site (ERMCS)[44,45]. Proteins involved in mitochondrial fission and fusion machineries, including DRP1 and mitofusins, converge near ERMCSs, establishing hotspots of heightened membrane dynamics[46]. The spatial coordination of ERMCS enables rapid responses to metabolic signals, highlighting the dynamic control of mitochondrial activity on their shape[46]. A plethora of tethering protein complexes are involved in constituting the mammalian ERMCS[47,48], including MFN1/2[49] and the IP3R-Grp75-VDAC1-MCU axis[50,51]. In addition to the aforementioned functions, ERMCSs can regulate many other biological processes, including lipid synthesis and transfer[52], and notably, Ca^{2+} exchange between organelles[53]. ERMCSs also act as the structural foundation of signaling hubs that interplay with multiple regulatory pathways, such as the mTORC2-AKT pathway, to regulate cell growth and metabolism[54,55]. For decades, overwhelming evidence has emphasized the indispensability of proper ERMCS function in cells by linking it to the pathogenesis of various human diseases, such as cancer[56,57], type-II diabetes mellitus[58], and neurodegeneration[59].

In this study, we bridged these ideas and utilized *Drosophila* and mammalian cell lines to investigate the significance of 40S ribosomal subunit recycling in translational quality control. We found that Usp10 and rin in *Drosophila* and their orthologs USP10 and G3BP1 in human cells can significantly impact mitochondrial homeostasis. The 40S ribosomal subunit recycling complex, in which Usp10/USP10 and rin/G3BP1 reside, colocalizes at mitochondrial fission-fusion hotspots, thereby precisely modulating mitochondrial dynamics according to metabolic fluctuations. The Usp10-rin/USP10-G3BP1 complex is mechanistically associated with ERMCS and regulates Ca^{2+} transfer to mitochondria by affecting its assembly. The ERMCS activity change influences the activities of both mTORC1 and mTORC2. Two genetic modifiers, *Fmr1* and *dZnf598*, were identified. Fmr1 was found to be physically integrated into the Usp10-mTORC2-ERMCS superstructure. The findings uncover a link between translational quality control and mitochondrial physiology. We demonstrate a function of the 40S ribosomal subunit recycling process after the RQC, highlighting its role as a signaling hub communicating with broader metabolic pathways to precisely reshape mitochondrial homeostasis and cellular energy metabolism to cope with ribotoxic stress induced by translational stagnation.

Results

40S ribosomal subunit recycling factors Usp10/USP10 and rin/G3BP1 regulate mitochondrial morphology

The first step in recycling the 40S ribosomal subunit is deubiquitination facilitated by the G3BP1-Family-USP10 complex to prevent lysosomal degradation[27]. It has not yet been determined whether the 40S ribosomal subunit released during RQC has functions beyond translation. To investigate the biological significance of this mechanism, we tuned the expression levels of two core genes in *Drosophila*, *Usp10* (the ortholog of *USP10*) and *rin* (the ortholog of *G3BP1*). We first found that their appropriate expression is of great significance to the organism's adaptability to stress. Overexpression (OE) or knockdown of the whole animal (driven by *Act5C-Gal4* or *Daughterless-Gal4*), pan-neuronal tissue (driven by *1407-Gal4*, *Elav-Gal4*) and mesoderm (driven by *24B-Gal4*) caused a severe decline in their offspring fitness, such as death or a severe decrease in population numbers, as well as significantly shortened lifespan of escapees (Supplementary Data 1). We observed that the *MHC-Gal4* driver, when expressed in muscle, effectively produces visible phenotypes through the OE of target genes, while knockdown does not result in lethality. The efficiencies of gene overexpression and knockdown used in Figs. 1–7 are depicted in Figs. 3i, 4a, 4b, 5g, and Supplementary Fig. 3g. It was reported that administration of sulfaquinoxaline and apigenin induces readthrough of eukaryotic translation[60], which leads to RQC and the subsequent ubiquitination on

https://doi.org/10.1038/s41467-025-56346-3

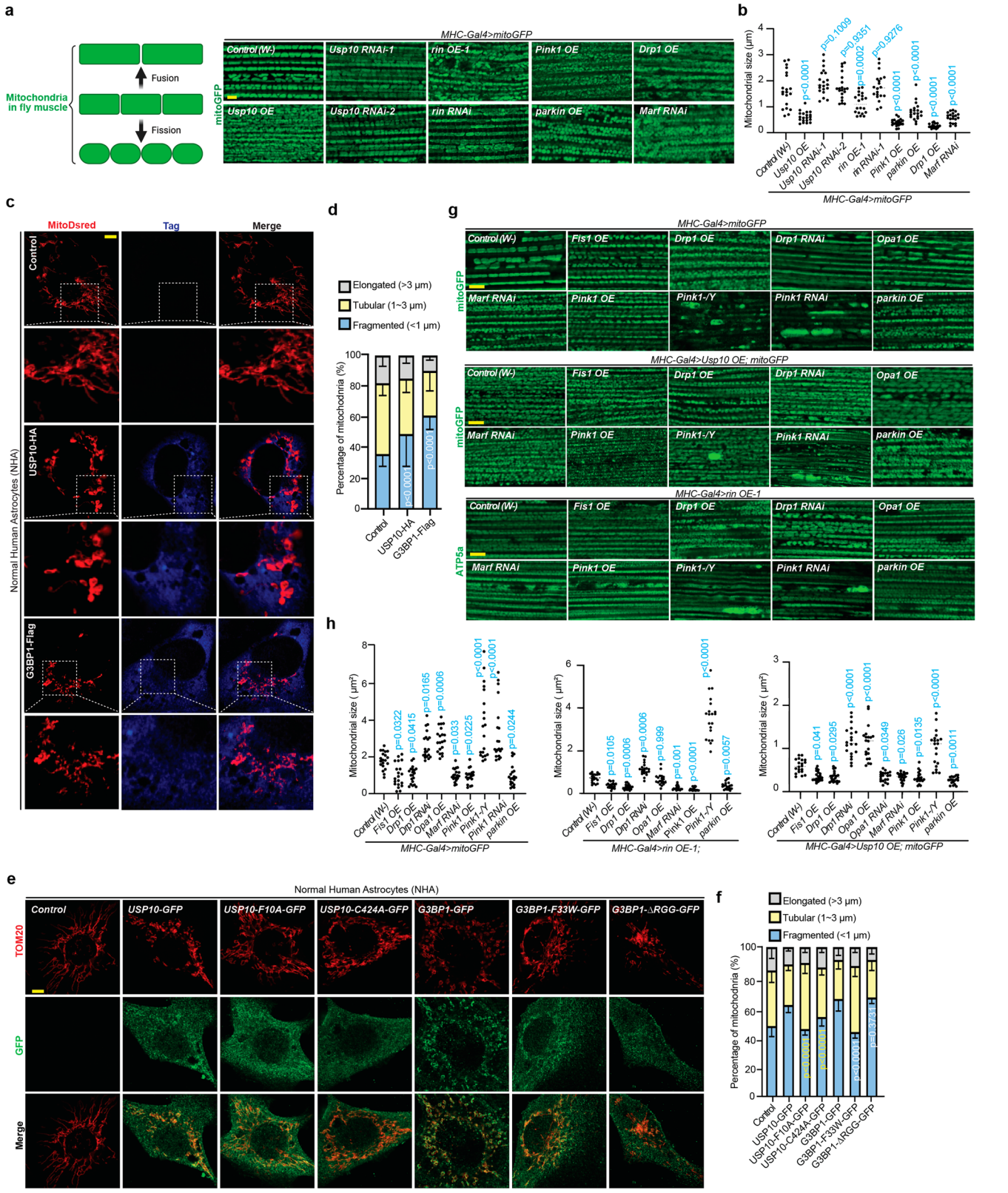

ribosomal small subunit proteins (RpS). It was discovered that OE of *Usp10* and *rin* counteracted the toxicity of apigenin and sulfaquinoxaline, leading to an extension in lifespan (Supplementary Fig. 1a, b). As a downstream event of RQC, the activity change of the 40S ribosomal subunit recycling complex should not impact the incidence of translation stalling. This aligns with our observation that no alterations in ribosome stalling events were noted during experiments involving puromycin labeling of stalled nascent peptides in *Drosophila* and normal human astrocyte (NHA) cells, a non-cancerous cell type (Supplementary Fig. 1c)[61]. However, they are capable of effectively eliminating ubiquitination on the RpS subunit and increasing the stoichiometric ratio of the RpS subunit/RpL subunit, thus indicating more efficient 40S ribosomal subunit recycling (Supplementary Fig. 1d–g). On the contrary, RNAi flies were more sensitive to translational readthrough-

Fig. 1 | Usp10/USP10 and rin/G3BP1 influence mitochondrial dynamics. a A cartoon (Left) explaining the expected changes in *Drosophila* muscle mitochondria under regulation of mitochondrial fission/fusion. Immunostaining (Right) showing changes in mitochondrial morphology in fly muscle tissue, regulated by Usp10 and rin. OE, overexpression; RNAi, RNA interference. Control (*w*-) serves as a negative control; *Pink1 OE*, *parkin OE*, *Marf RNAi*, and *Drp1-HA* serve as positive controls. Mitochondrial morphology is visualized using mitoGFP. **b** Quantification of mitochondrial size shown in **a** Mitochondria counts were obtained from three samples ($n = 3$, 7 areas counted per sample. Biologically independent, same for all samples/repeats/experiments). **c** Immunostaining of mitoDsRed (a mitochondrial marker) and tagged proteins (HA/Flag) showing the effects of ectopic expression of USP10 and G3BP1 on mitochondrial morphology in NHA cells. The white dashed line indicates the enlarged section below. **d** Quantification of images shown in **c** Cell counts were obtained from six independent experiments ($n = 6$, 15 areas counted per experiment). **e** Immunostaining of TOM20 (a mitochondrial marker) and GFP (protein tag) showing the effects of various mutants of USP10 (F10A, C424A) and G3BP1 (F33W, ΔRGG) on mitochondrial morphology in NHA cells. **f** Quantification of images shown in **e**. Cell counts were obtained from six experiments ($n = 6$, 15 areas counted per experiment). Yellow *p* values, compared to USP10-GFP; white *p* values, compared to G3BP1-GFP. **g** Immunostaining of mitochondrial markers showing the regulation of mitochondrial fission/fusion genes in muscle tissue of the control, *Usp10*, and *rin* OE flies. Control (*w*-) serves as a negative control in each genetic background. Mitochondrial morphology is visualized by mitoGFP (control and *Usp10* group) and ATP5α (*rin* group). **h** Quantification of mitochondrial size shown in **g**. Mitochondria counts were obtained from three samples ($n = 3$, 7 areas counted per sample). One-way ANOVA test (two-sided) followed by post hoc Dunnett's multiple comparisons test 95% confidence interval (CI) was used in **b**, **h**. All scale bars, 5 μm. Data are means ± SEM. The *p* values are included in the figure. Source data are provided as a Source Data file.

triggered ribotoxicity, as evidenced by increased ubiquitination on RpS subunits (Supplementary Fig. 1d–g).

When investigating the physiological functions of Usp10 and rin, it was observed that they strongly impacted mitochondrial morphology in the *Drosophila* indirect flight musculature. The strong mitochondrial fragmentation observed upon OE of either one of them resembles the mitochondrial morphology found in muscles when *Drp1* and *Pink1* are overactivated, or *Marf* is knocked down (Fig. 1a, b). *Usp10* and *rin* OE in *Drosophila* dopaminergic neurons also significantly changed mitochondrial morphology, characterized by the presence of swollen mitochondria or thin and disorganized mitochondrial networks (Supplementary Fig. 2a, b). While some enlarged mitochondria were noted, this does not necessarily indicate a contrasting regulation, as swollen mitochondria were also observed in *Pink1* OE flies. Instead, it suggests that mitochondria in various tissues respond differently to excessive fission and that their morphology is intricately regulated.

The regulation of mitochondrial dynamics by USP10 and G3BP1 is also conserved in human cells. Akin to the effects seen in flies, in NHA cells, OE of *USP10* and *G3BP1* significantly increased the proportion of fragmented mitochondria (Fig. 1c, d). To determine how USP10 deubiquitination activity and its interaction with G3BP1 affect mitochondrial dynamics, different mutants of USP10 and G3BP1 were introduced into NHA cells. They included USP10 F10A (unable to bind to G3BP1), USP10 C424A (enzyme-inactive), G3BP1 F33W (unable to bind to USP10), and G3BP1-ΔRGG (unable to bind to the 40S ribosomal subunit)[34]. This experiment found that USP10 F10A, USP10 C424A, and G3BP1 F33W significantly lost their ability to promote mitochondrial fission, whereas G3BP1-ΔRGG remained unaffected. This suggests that the function of USP10 and its interaction with G3BP1 are important for this regulation, but the binding of G3BP1 to the 40S ribosomal subunit does not appear to be essential (Fig. 1e, f). These conclusions were further supported by investigating a series of truncations of USP10 in NHA cells. Our data indicate that the N-terminal USP10-G3BP1/p53 binding domain (aa. 2-116) and the C-terminal USP domain (aa. 410-789) are involved in the functional regulation of mitochondrial morphology. Expression of these truncations alone induced mitochondrial fragmentation, whereas the addition of the middle-disordered region (aa. 117-274) did not (Supplementary Fig. 2c, d), suggesting a potential multi-faceted effect. Interestingly, in HeLa cells stably expressing GFP-Parkin, OE of both *USP10* and *G3BP1* induced mitochondrial fragmentation and altered their distributions, towards a more concentrated perinuclear pattern. This effect was largely attenuated in HeLa cells lacking endogenous Parkin expression, suggesting a potential functional role of the PINK1-Parkin pathway in regulating mitochondrial morphology (Supplementary Fig. 3a–d).

We next wanted to elucidate the interaction between *Usp10, rin*, and fission-fusion genes involved in regulating mitochondrial dynamics. Our data revealed that genes controlling mitochondrial dynamics, such as *Drp1*, *Opa1*, *Marf*, *Pink1*, and *parkin*, showed strong genetic interactions with *Usp10* and *rin* in regulating mitochondrial morphology in fly musculature[62]. That is, under the fission-promoting regulations (*e.g.*, OE of *Drp1*, *Fis1*, *Pink1* or *parkin*, and RNAi of *Opa1* or *Marf*), *Usp10* and *rin* OE exhibited enhanced effects, whereas under the fission-inhibiting regulations (*e.g.*, knockdown of *Drp1*, *Fis1*, *Pink1* or *parkin*, and OE of *Opa1* or *Marf*), their effects were significantly alleviated (Fig. 1g, h). Previous studies have reported that increased mitochondrial fission aids in resolving mitochondrial aggregation in *Pink1* loss-of-function flies[62,63]. Consequently, we proceeded to examine whether *Usp10* and *rin* have similar capabilities. Consistent with our expectations, *Usp10* and *rin* OE effectively splintered fused mitochondria in the *Pink1* RNAi fly muscle tissue, while their RNAs increased the size of fused mitochondria (Supplementary Fig. 3e, f). However, unlike previously confirmed fission genes, OE of *Usp10* and *rin* failed to successfully remove aggregated mitochondria (indicated by the persistence of bright signals of mitoGFP, mitochondrial-targeted GFP reporter), suggesting a lack of promotion of downstream mitophagy.

In addition to their roles in the 40S ribosomal subunit recycling, USP10 and G3BP1 have been shown to co-assemble and predominantly regulate the formation and function of stress granules[33,34,64,65]. To assess the impact of stress granule formation on mitochondria, we first examined two key hallmarks of stress granules, rin and Fmr1 (Fragile X messenger ribonucleoprotein 1 protein, the *Drosophila* ortholog of human FMRP), in *Usp10* and *rin* OE flies[34,66]. Unlike in human cells, OE of stress granule core components such as Usp10, rin and Rox8 (the *Drosophila* ortholog of human TIA-1)[67] in fly muscle tissue did not sufficiently induce significant stress granule formation (Supplementary Fig. 4a, b), despite the presence of elevated phospho-Ser51-eIF2α signals (Supplementary Fig. 4c). This result suggests that alterations in mitochondrial morphology are not triggered by stress granule formation. No punctate stress granules were observed in *Pink1 RNAi* and *parkin* mutant flies, hinting that dysfunctional mitochondria lead to translational arrest but may not sufficiently induce stress granule assembly[13] (Supplementary Fig. 4d). Altogether, our findings indicate that increased activity of Usp10 and rin heightens mitochondrial fission. This prompts further investigation into the mechanistic role of 40S ribosomal subunit recycling in mitochondrial dynamics.

The 40S ribosomal recycling complex contacts fission-fusion machineries at the mitochondrial dynamic hotspots

The maintenance of steady-state mitochondrial morphology relies on a delicate equilibrium between fission and fusion events. The fission and fusion machineries co-localize to create hotspots of membrane dynamics associated with the endoplasmic reticulum (ER) that may respond rapidly to metabolic changes[46]. Given that Usp10 and rin can influence mitochondrial morphology, is it possible that they regulate mitochondrial dynamics through their influence on the organization of mitochondrial dynamic hotspots? Immunostaining was first conducted in fly muscles to detect Drp1 (the *Drosophila* ortholog of

human DRP1) and Marf (the *Drosophila* ortholog of human MFN1 and MFN2). The Drp1 signals surrounding mitochondria were found to be strongly elevated in *Usp10* and *rin* OE flies, while remaining stable or slightly reduced in flies with *Usp10* and *rin* knockdown (Supplementary Fig. 5a). Marf signals were also concentrated in the proximity of mitochondria, albeit displaying only minor fluctuations in intensity (Supplementary Fig. 5b). Notably, the components of the mitochondrial fission-fusion machinery in *Drosophila*, similar to those found in human cells[46], are positioned closer to bona fide ER contact sites rather than mitochondria, as evidenced by stronger and more clustered signals of ER (KDEL-GFP) in *Usp10* and *rin* OE cases (Supplementary Fig. 5a, b). Moreover, a significant augmentation in the co-localization of DRP1 with mitochondria (mitoDsRed) was discerned in NHA cells upon the OE of USP10 and G3BP1, indicating the potential influence of 40S ribosome subunit recycling complex on mitochondrial dynamics (Fig. 2a–c). In contrast, no significant change was observed in the mitochondrial colocalization of MFN1 (Supplementary Fig. 5c–e) and MFN2 (Supplementary Fig. 5f–h), suggesting that this remodeling may be more inclined towards promoting fission.

We next employed the proximity ligation assays (PLAs, Duolink®) to validate possible close interactions between components of the 40S ribosomal recycling complex and fission-fusion machineries in situ[68]. To circumvent antibody specificity concerns, we used a genomic knock-in line of Marf (*Marf-HA KI*) and a low-expression line of Drp1 (*Drp1-HA*, which does not change mitochondrial size in a wild type, shown in Fig. 2j) to elucidate the site of convergence of fission-fusion machineries[69]. It was observed that Usp10 and RpS10 (ribosomal small subunit protein 10) are closely associated with Marf (Fig. 2d–g) and Drp1 (Fig. 2h–k), and *Usp10* OE could enhance the interaction. rin also closely associated with Marf and Drp1; however, its interaction was not strengthened by *Usp10* OE (Supplementary Fig. 6a–d). In contrast, no interactions were detected between RpL7a (ribosomal large subunit protein 7a) and Marf and Drp1 (Supplementary Fig. 6e,f), or between Marf and Clbn (Supplementary Fig. 6g), hinting that after RQC, the 40S ribosomal subunit recycling complex, rather than the CAT-tailing complex, is more likely to interact with the fission-fusion machineries. This result offers compelling insights into the changes seen in mitochondrial morphology and functions under pathological conditions. For example, in *Drosophila* and NHA cells, mitochondrial fragmentation was noted after being exposed to emetine (a translational inhibitor)[70] and SULFAQUINOXALINE (a readthrough inducer), mirroring the effect of CCCP (a mitochondrial uncoupler) (Supplementary Fig. 6h–k). Furthermore, the short-term administration of sulfaquinoxaline also led to a notable decrease in mitochondrial respiratory efficiency (Supplementary Fig. 6l, m).

To dissect the molecular mechanism thoroughly, we next analyzed the complex consisting of 40S ribosomal subunit recycling factors and fission-fusion machineries using tandem co-immunoprecipitation (co-IP). Tandem co-IP consists of two consecutive co-IP steps using antibodies against HA tag (first round targeting Marf-HA) and endogenous rin (second round targeting rin) to achieve a high-quality affinity separation of protein-containing complexes under the native expression conditions[71]. Our assays showed that i) *Usp10* OE increases the binding between rin and Marf, thereby strengthening the 40S ribosomal subunit recycling-Marf complex; ii) ASCC2 is more evident when *Usp10* expression is enhanced, indicating a potential early interaction with the RQT complex that persists with Usp10 and rin; iii) The absence of Clbn implied that the 60S ribosomal subunit and the CAT-tailing complex are not recruited simultaneously; iv) Consistent with these findings, RpS but not RpL proteins, were identified (Fig. 2l). Interestingly, signals from Hsc70-5 (the *Drosophila* homolog of human HSPA9/GRP75)[57] were not detected in this complex. This indicates that the 40S ribosomal subunit recycling complex interacts autonomously with fission-fusion molecules[46] and endoplasmic reticulum-mitochondria contact sites (ERMCSs), despite the concentration of these factors at the contact area between ER and mitochondria (Fig. 2m). Thus, Usp10 and rin, members of the 40S ribosomal subunit recycling complex, primarily regulate mitochondrial morphology through their interaction with the mitochondrial fission and fusion mechanisms.

Usp10/USP10 and rin/G3BP1 regulate mitochondrial homeostasis

To deepen our understanding of the role of the 40S ribosomal subunit recycling process in sustaining mitochondrial homeostasis, we first assessed the wing posture of *Drosophila*. The indirect flight muscles are responsive to mitochondrial functions, and any disturbances in mitochondrial homeostasis, such as mitochondrial fission/fusion imbalance or mitophagy deficiency, can lead to noticeable wing posture failure, as seen in *Drosophila* models of Parkinson's disease[62,72,73]. Comparable to the *Pink1* mutant, OE of *Usp10* and *rin* exhibited similar failure in wing posture and reduced ATP levels, indicating a compromise in mitochondrial function (Fig. 3a, b). The study also revealed that Usp10 seems to have a more pronounced impact on this regulation, evidenced by the partial mitigation of *rin* OE effects with *Usp10* RNAi. On the other hand, *rin* RNAi was unable to reverse the *Usp10* OE effects (Supplementary Fig. 7a, b). This could also clarify the greater effects of Usp10 compared to rin. Transmission electron microscopy (TEM) examination of fly indirect flight muscle tissue unveiled degeneration of fascicles (myofiber bundles) and abnormalities in mitochondrial ultrastructure, including cristae loss in *Usp10* OE and myeloid-like structures in *rin* OE flies, which might be the traces of degeneration and a result of organelle and membrane lipid breakdown (Fig. 3c). Curiously, *Usp10* RNAi also displayed aberrantly shaped (curved or concentric) cristae, indicating the significance of Usp10 balance in preserving normal mitochondrial cristae architecture (Supplementary Fig. 7c).

The integrity of cristae is linked to the assembly of the mitochondrial respiratory chain complexes[74]. The Blue Native Polyacrylamide Gel Electrophoresis (BN-PAGE) revealed that the assembly of mitochondrial respiratory chain complexes -I, -V, -II and the supercomplexes were significantly compromised in *Usp10* and *rin* OE flies (Fig. 3d), as indicated by the diminished blue bands at their respective positions, echoing the changes in ATP production. Malfunctions in the respiratory chain complex assembly are often accompanied by elevated levels of reactive oxygen species (ROS)[74]. Indeed, utilizing mito-roGFP2[75] (a mitochondrial redox sensor) and mitoSOX[76] (a mitochondrial superoxide dye) as indicators of redox status within mitochondria, we recorded notably increased signals in *Usp10* and *rin* OE flies (Fig. 3e, f, Supplementary Fig. 7d, e). The mitochondrial membrane potential also serves as a vital indicator of mitochondrial activity, reflecting the functionality of respiratory chain complexes and the effectiveness of electron transport and oxidative phosphorylation. We detected a higher mitochondrial membrane potential in JC-10[77] staining of *Usp10* and *rin* OE flies, while a minor yet significant reduction in membrane potential was noted in flies with RNAi knockdown of these genes (Fig. 3g, h). This suggests a partial decoupling of mitochondrial oxidative phosphorylation and ion gradients across the mitochondrial inner membrane. These clues prompt further investigation of the mechanism that underlies this paradox.

Dysfunction of respiratory chain complexes and a decrease of membrane potential typically lead to mitochondrial damage, which in turn triggers mitophagy, primarily via the canonical branch of the PINK1-Parkin-mediated pathway[72,78]. Nevertheless, the substantial accumulation of damaged mitochondria in *Usp10* OE flies seems to indicate a disruption in mitophagy. We used an ectopically expressed mitochondrial quality control (mitoQC) indicator to visualize the occurrence of mitophagy in fly muscle tissue[79]. In *Usp10* and *rin* OE flies, no perceivable increase in mito-lysosomes was found, as

https://doi.org/10.1038/s41467-025-56346-3

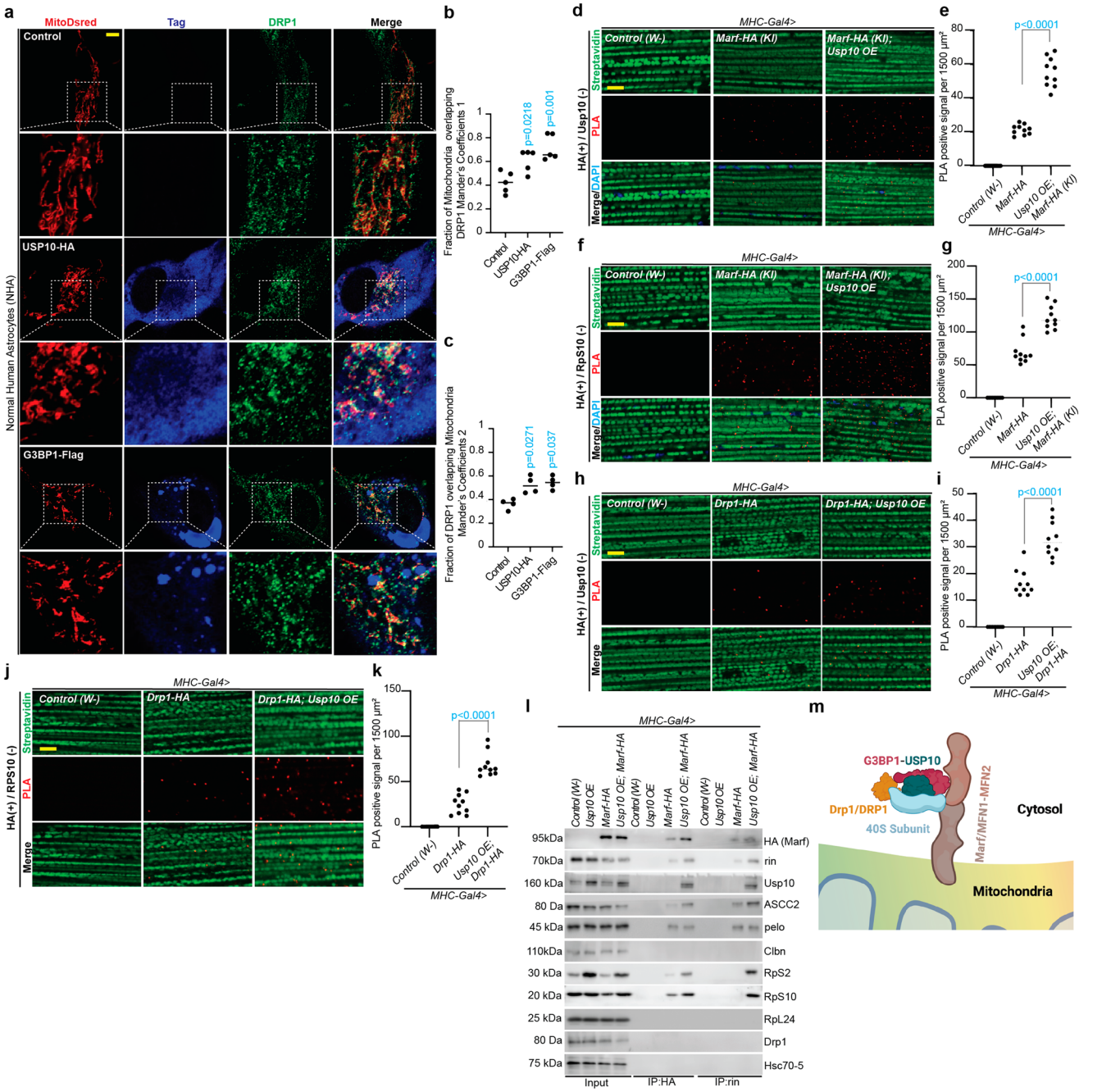

Fig. 2 | The 40S ribosomal subunit recycling complex interacts with the mitochondrial fission-fusion machineries. a Immunostaining of DRP1, mitoDsRed, and tagged proteins (HA/Flag) showing the impact of USP10 and G3BP1 on the colocalization of DRP1 with mitochondria in NHA cells. **b, c** Quantification of images shown in **a** Mander's overlap coefficients MC1 (colocalization of DRP1 with mitochondria) in **b**; MC2 (colocalization of mitochondria with DRP1) in **c** Measurements were calculated from five experiments ($n = 5$) in **b**, and four ($n = 4$) in (**c**). One-way ANOVA test (two-sided) followed by post hoc Dunnett's multiple comparisons test 95% confidence interval (CI). **d** Proximity ligation assay (PLA) detection of Marf-HA(+)/Usp10(-) interaction (red puncta), showing increased binding in *Usp10* OE flies. Mitochondria are shown in green (streptavidin labeling) in (**d**, **f**, **h**, **j**). KI, genomic knock-in. **e** Quantification of images shown in (**d**). **f** PLA detection of Marf-HA(+)/RpS10(-) interaction (red puncta), showing increased binding in *Usp10* OE flies. **g** Quantification of images shown in (**f**). **h** PLA detection of Drp1-HA(+)/Usp10(-) interaction (red puncta), showing increased binding in *Usp10* OE flies. **i** Quantification of images shown in (**h**). **j** PLA detection of Drp1-HA(+)/RpS10(-) interactions (red puncta), showing increased binding in *Usp10* OE flies. **k** Quantification of images shown in (**j**). Data were obtained from ten samples ($n = 10$) in (**e**, **g**, **i**, **k**). Two-tailed Student's t-test was used with a 95% confidence interval (CI) in (**e**, **g**, **i**, **k l**). Tandem co-IP analysis using HA tag (for Marf-HA) and rin antibodies in sequence, showing the interacting proteins within the same complex in control and *Usp10* OE flies. Control (*w*-) serves as a negative control. Three experiments ($n = 3$) were conducted. **m** A working model illustrating the interactions between the 40S ribosomal subunit recycling complex and mitochondrial fission/fusion proteins Drp1 and Marf. The figure was created in BioRender[134]. All scale bars, 5 µm. The *p* values are included in the figure. Source data are provided as a Source Data file.

https://doi.org/10.1038/s41467-025-56346-3

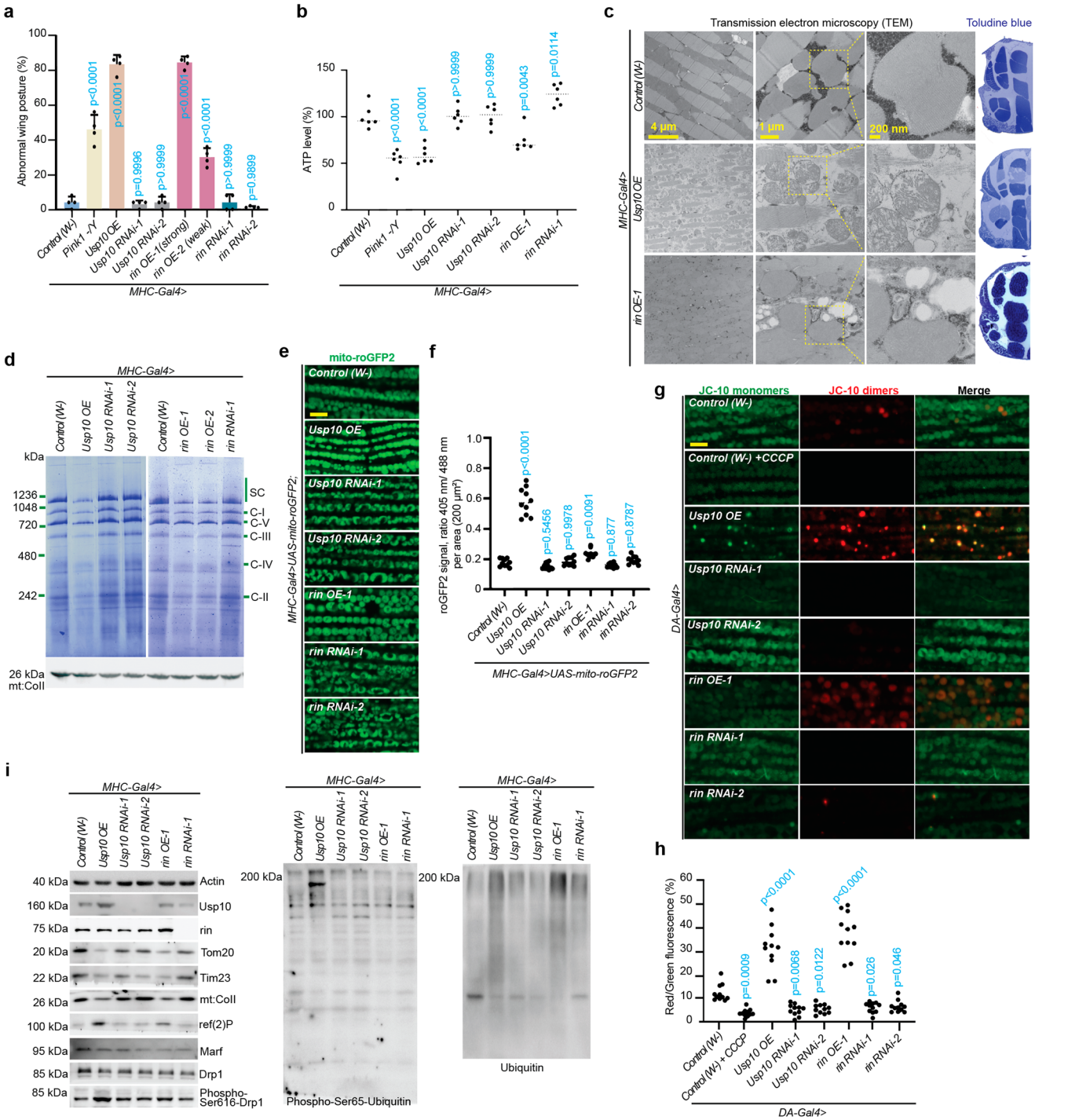

Fig. 3 | Usp10/USP10 and rin/G3BP1 regulate mitochondrial activities. **a** Standardized wing posture assay showing the effects of Usp10 and rin in the fly indirect flight muscle. 25 flies were examined per group; four groups ($n = 4$) were counted per genotype. Control (*w-*) serves as a negative control; *Pink1-/Y* serves as a positive control. **b** Standardized ATP measurements (normalized to the Control) on fly muscle samples showing the effects of Usp10 and rin on energy production. 5 male flies were used per sample; six samples ($n = 6$) were measured per genotype. **c** Transmission electron microscopy (TEM, left) and Toluidine blue staining (right) images showing the effects of Usp10 and rin on mitochondrial ultrastructure in *Drosophila* indirect flight muscle tissue. The boxed regions are magnified in the right panel. Five samples ($n = 5$) were analyzed. **d** BN-PAGE analysis showing the regulation of mitochondrial respiratory chain complex assembly by Usp10 and rin. Control (*w-*) serves as a negative control; mt:COII is a loading control for BN-PAGE. The signal intensity of the corresponding band indicates the assembly of the complex. Three experiments ($n = 3$) were conducted. **e** Mito-roGFP2 imaging in fly muscle tissue showing the mitochondrial redox status modulation by Usp10 and rin. **f** Quantification of images shown in (**e**). An increase in the 405 nm/488 nm ratio indicates elevated oxidative stress. Ten samples ($n = 10$) were analyzed. **g** JC-10 staining in fly muscle tissue showing the mitochondrial membrane potential modulation by Usp10 and rin. **h** Quantification of images shown in (**g**). An increased red /green ratio indicates elevated mitochondrial membrane potential; vice versa. Eleven samples ($n = 11$) were analyzed. **i** Immunoblotting showing changes in mitochondrial, fission/fusion, and mitophagy markers affected by Usp10 and rin. Control (*w-*) serves as a negative control; Actin is used as a loading control in blots. All scale bars, 5 µm, except in **c** One-way ANOVA test (two-sided) followed by post hoc Dunnett's multiple comparisons test 95% confidence interval (CI) was used in (**a**, **b**, **f**, **h**). Data are means ± SEM. The *p* values are included in the figure. Source data are provided as a Source Data file.

indicated by a "spectral shifted" (from green to red) puncta signal under acidic conditions. In contrast, a noticeable rise in mitolysosomes was seen in the positive controls of *Pink1* and *parkin* OE flies (Supplementary Fig. 7f, g). Due to the mitophagy blockage, in *Usp10* and *rin* OE flies, reductions in several mitochondrial markers (*e.g.*, mt:CoII, Tom20, and Tim23) and accumulation of autophagy indicators (*e.g.*, ref(2)P, the *Drosophila* homolog of human SQSTM1/p62, polyubiquitin, and phospho-Ser65-ubiquitin (only in *Usp10* OE)) (Fig. 3i). Of note, while the total amount of Drp1 remained constant, the level of phospho-Ser616-Drp1 increased significantly when the 40S ribosomal subunit recycling process was excessively activated, echoing the previous finding, a shift towards mitochondrial fission.

Simultaneously, the accumulation of ref(2)P and polyubiquitin, along with ubiquitin Ser65 phosphorylation, was also detected in the immunostaining of *Usp10* and *rin* OE flies. The *Usp10* and *rin* OE flies notably increased the prominent punctate signals of ref(2)P, polyubiquitin, and phospho-Ser65-ubiquitin (Supplementary Fig. 8a, b). It was observed that *Usp10* and *rin RNAi* flies showed minimal divergence from the controls, but displayed a lack of ref(2)P accumulation, while ubiquitin accumulation remained unaffected following sulfaquinoxaline and apigenin treatments (Supplementary Fig. 8c). The ref(2)P protein is an important autophagy mediator in *Drosophila*, which links accumulated polyubiquitin signals to downstream autophagic processes such as mitophagy, ribophagy[80], and aggrephagy[81]. Therefore, the loss of function of *Usp10* and *rin* would result in a diminished stress response, ultimately leading to a decline in the fitness of flies. In conclusion, the roles of Usp10 and rin are essential for maintaining mitochondrial homeostasis. Either an excess or a deficiency of these factors can arouse profound changes in mitochondrial function and homeostasis.

Identification of interactors associated with the 40S ribosomal subunit recycling complex

Increased fission usually facilitates the engulfment in mitophagy, leading to the removal of damaged mitochondria and the maintenance of cellular mitochondrial health[62,82]. However, mitochondrial fission in *Usp10* and *rin* OE flies was accompanied by both ultrastructural and functional abnormalities, as well as hindrance of mitophagy, indicating the presence of intricate regulatory mechanisms. To reconcile the discrepancy between observational data and theoretical predictions, genetic screening and proteomic analysis were both employed to dissect the impact of activating the 40S ribosomal subunit recycling pathway on *Drosophila* metabolism (Supplementary Fig. 9a). Exploiting the UAS-Gal4 system, a genetic screen was conducted with the mitochondrial morphology as a readout (as described in the **Methods** section)[83,84]. Due to the heightened phenotype displayed in *Usp10* OE, our initial screening was conducted in this genetic background. We selected candidates previously implicated in genetics interactions with *USP10/Usp10*, along with genes associated with RNA quality surveillance, mitochondrial quality control, and metabolic regulation, as potential candidates for further investigation[36–40,85–87]. In this screen, dZnf598, Fmr1[88], mitochondrial-fission fusion genes, ERMCS constituents, and components of mTORC1/2 complexes were identified as strong genetic modifiers. These genetic modifiers displayed consistent behavior in *rin* OE flies (Supplementary Data 2).

In our prior immunoblot analysis on *Usp10* and *rin* flies, we found that the expression of specific proteins, such as mitochondrial proteins and autophagy receptors, was significantly tuned (Fig. 3i). Here, their proteomes were analyzed to identify proteins that are regulated, and the data was cross-validated through comparison with results from genetic screens mentioned above. *Drosophila* thoracic samples were obtained from *Usp10* (Usp10 OE, $n = 3$; Usp10 RNAi, $n = 3$) and *rin* (rin OE, $n = 3$; rin RNAi, $n = 3$) flies crossed with *MHC-Gal4* driver, and were subsequently compared to a control group (*MHC-Gal4/w-*, $n = 3$). A quantitative analysis of total tryptic digests labeled with Tandem Mass Tag (TMT) was performed using liquid chromatography coupled with tandem mass spectrometry (LC-MS/MS). The mass spectra were queried against the UniProt *Drosophila Melanogaster* protein database to ascertain peptides and their respective proteins. A total of 3196 proteins were identified and analyzed (Supplementary Data 3). After normalization and batch effect correction procedures, diverse sample groups demonstrated effective separation, as demonstrated by principal component analysis (PCA) (Supplementary Fig. 9b). Akin to previous observations, it was noted that Usp10 OE and rin OE samples exhibited greater proteomic changes in comparison to the control group, whereas RNAi samples had lesser effects (Fig. 4a, b, Supplementary Data 4).

Next, we undertook a thorough comparison of proteins that were expressed differentially between the experimental and control groups. Relative fold changes in protein amounts across different genotypes were represented as volcano plots, showing the statistical significance (FDR < 0.05) and normalized ratios ($|\log2(FC)| > 0.323$) in accordance with previous studies[89–91]. This proteomic analysis focused on pathways conserved in humans (mammals). While several regulatory pathways specific to arthropods exhibited pronounced changes, they would not be our primary targets. Their analyses are presented in the discussion. The levels of Usp10 and rin proteins were found to fluctuate according to overexpression or knockdown within the respective groups. This signifies the effectiveness of gene regulation in the samples, a prerequisite for subsequent successful analysis of pathways. Proteins showing alterations in immunoblotting (Fig. 3i) were still identified as undergoing changes in proteome analysis (Fig. 4a), including a decrease in mitochondrial proteins (green dots) and an increase in ref2(P). Proteins within RQC and other RNA metabolism-related pathways were also regulated, including dZnf598, Clbn, and Fmr1, which also corroborated our findings from genetic screening.

The proteins exhibiting differential expression in each comparison were subjected to the gene set enrichment analysis (GSEA) to highlight molecular pathways affected by *Usp10* and *rin*[92]. Pathways with an FDR of less than 0.05 were characterized and annotated in each genotype. Substantial alterations in pathways related to translation or ribosome homeostasis were found in the Usp10 OE and Rin OE groups, including cap-dependent translation initiation, eukaryotic translation initiation, and formation of a reservoir of free 40S subunits (Fig. 4c, d). These modifications align with the established role of the USP10-G3BP1 complex in the recycling of the 40S ribosomal subunit[27], and further validate the efficacy of our proteomic analysis approach. Modifications in the P53 regulatory pathway correlated with USP10 were also discerned (Fig. 4e)[87,93]. Furthermore, we observed enrichment of the autophagy and mTOR signaling pathways, aligning with the findings of genetic analysis (Fig. 4f, g, Supplementary Data 5). The constituent proteins of ERMCS were not observed in the proteomic GSEA, possibly due to regulation taking place at the functional level. To summarize, through the integration of genetic screens and proteomic analyses, we have verified the known impacts of Usp10 and rin on mitochondrial homeostasis, and also unveiled components including dZnf598, Fmr1, ERMCS, and mTOR genes.

dZnf598 and Fmr1 interact with the 40S ribosomal subunit recycling complex

Through prior analyses, dZnf598 and Fmr1 were identified as cofactors of Usp10 and rin. Following this, we studied how they interact with the Usp10-rin complex and their involvement in regulating mitochondrial homeostasis. *dZnf598* and *Fmr1* differ in their regulations of mitochondrial functions, as the *Fmr1* OE phenotypically induces abnormal wing posture and decreased ATP levels in flies, but *dZnf598* does not (Supplementary Fig. 10a, b). Nevertheless, OE or knockdown of either *Fmr1* or *dZnf598* did not affect the assembly of mitochondrial respiratory chain complexes (Supplementary Fig. 10c), indicating that the decrease in ATP levels in *Fmr1* OE is unrelated to respiration. No

https://doi.org/10.1038/s41467-025-56346-3

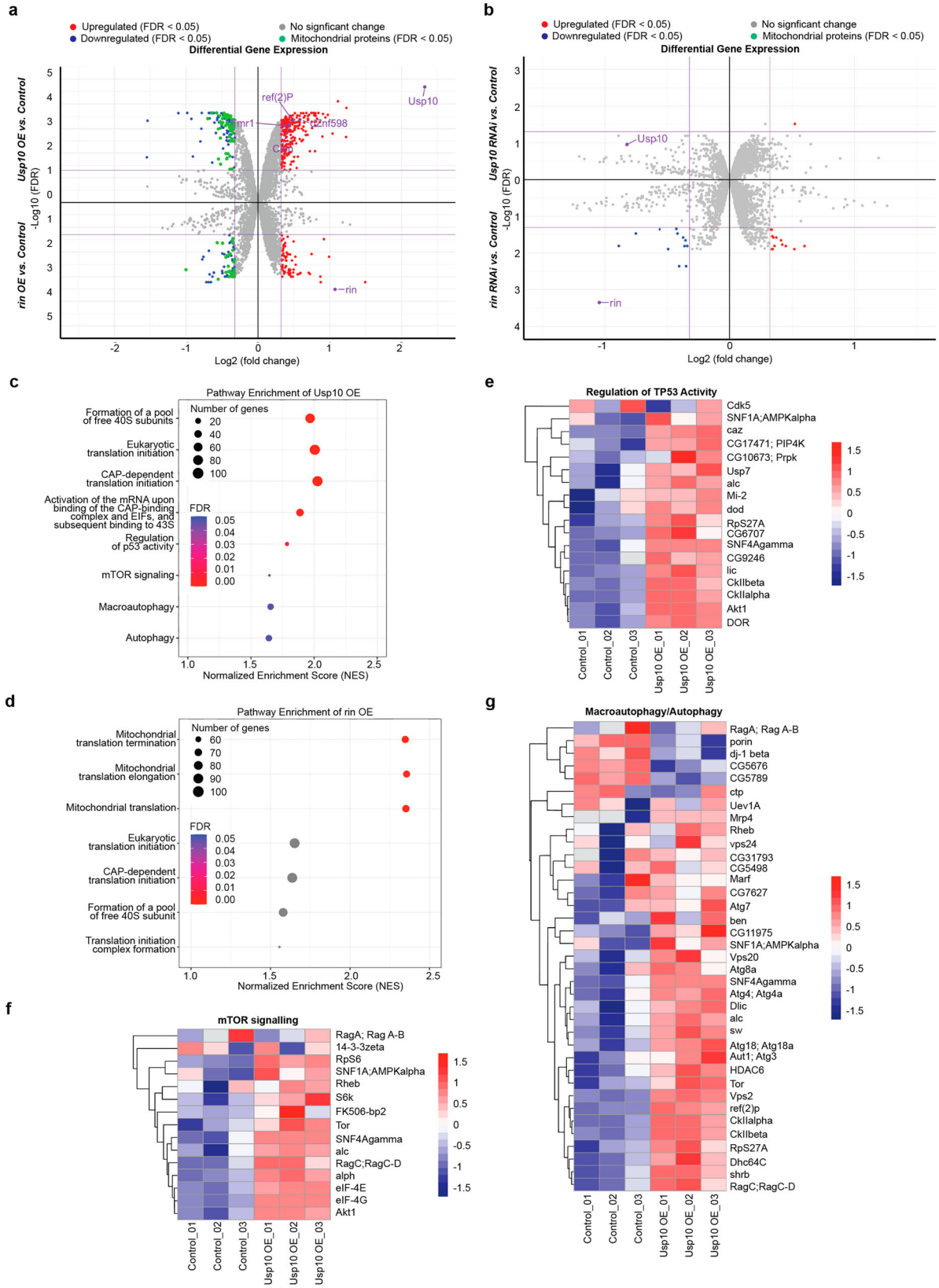

discernible changes in muscle mitochondrial morphology were seen when *dZnf598* and *Fmr1* were altered individually in wild-type flies (Supplementary Fig. 10d, e). However, these genes were able to influence the mitochondrial phenotype induced by *Usp10* and *rin* OE, with *dZnf598* OE exacerbating fragmentation and *Fmr1* OE reversing it (Fig. 5a, b). The discrepancy in their functions can be explained by their respective positions in the signal transduction cascade. Znf598 precedes the 40S subunit recycling, and its activation initiates a series of subsequent molecular events, while the role of Fmr1 is more intricate and will be elaborated later.

Interestingly, despite differing regulation of mitochondrial dynamics, *dZnf598* and *Fmr1* OE can both boost mitophagy. In line with

Fig. 4 | Identifying the interactors of the Usp10-rin recycling complex. a A dual volcano plot showing the log2 of fold changes and -log10 of FDR of proteins in Control (*MHC-Gal4 > w-*) vs. Usp10 OE (*MHC-Gal4>Usp10 OE*; the top half part) and Control (*MHC-Gal4 > w-*) vs. rin OE (*MHC-Gal4>rin OE*; the bottom half part) comparisons. Significantly upregulated (red) and downregulated (blue) genes are shown as colored dots. Significantly upregulated and downregulated mitochondrial genes are shown as green dots. The statistical significance threshold was FDR < 0.05, and the normalized ratio threshold was |log2(FC)| > 0.323. **b** A dual volcano plot showing the log2 of fold changes and -log10 of FDR of proteins in Control (*MHC-Gal4 > w-*) vs. Usp10 RNAi (*MHC-Gal4>Usp10-shRNA*; the top half part) and Control (*MHC-Gal4 > w-*) vs. rin RNAi (*MHC-Gal4>rin RNAi-2*; the bottom half part) comparisons. Significantly upregulated (red) and downregulated (blue) genes are shown as colored dots. The statistical significance threshold was FDR < 0.05, and the normalized ratio threshold was |log2(FC)| > 0.323. **c**, **d** Bubble plots showing the significant pathways from the pairwise Gene Set Enrichment Analysis (GSEA) comparison in Usp10 OE and rin OE groups. The vertical axis represents the pathway names, and the horizontal axis represents the normalized enrichment score. Pathways are ranked by their FDR from top to bottom. The FDR is depicted by the color of dots. A lower FDR value corresponds to a color closer to red, while a higher FDR value corresponds to a color closer to blue; gray indicates a lack of significance in the FDR value but ranks highly in the GSEA. The number of differentially expressed genes included in each pathway is illustrated by the size of the bubbles. **e**–**g** Heatmaps of gene sets (pathways) for "Regulation of TP53 activity" (**e**), "mTOR signaling" (**f**), and "Macroautophagy/Autophagy" (**g**), containing the expression levels of enriched genes in Control and Usp10 OE samples. The colors range from dark red to dark blue, representing the highest and lowest expression of genes, respectively. Source data are provided in the **Supplementary Data** files.

earlier studies, OE of *dZnf598* and *Fmr1* successfully eliminated mitochondrial aggregates in the muscle tissue of *Pink1* mutants (Fig. 5c, d)[94,95]. The OE of *dZnf598* and *Fmr1* also increased the presence of mito-lysosomes, suggesting a potential enhancement of mitophagy (Fig. 5e, f). The activation of mitophagy was further confirmed by immunoblot analysis. The OE of *dZnf598* and *Fmr1* effectively alleviated the abnormalities in mitochondrial proteins, including reducing the C-I30-u (an aberrant form of the complex-I 30 kDa subunit protein induced by mitochondrial stress), restoring the normal C-I30 level, and eliminating the ref(2)P accumulation. Conversely, the silencing of *dZnf598* and *Fmr1* by RNAi worsened these traits (Supplementary Fig. 10f). In TEM, *dZnf598* and *Fmr1* OE produced atypical cristae organization and recurrent myeloid structures in muscle tissues, reminiscent of those seen in *Usp10 RNAi* flies. Furthermore, we found mitochondria are engulfed by some myeloid structures, indicating the presence of increased mitophagy (Supplementary Fig. 10g). Vice versa, the *dZnf598* and *Fmr1* RNAi notably exacerbated phenotypes of *Pink1* mutants (Fig. 5c, d, Supplementary Fig. 10f), thus reaffirming their crucial involvement in regulating mitophagy. It was also found that the role of FMRP and ZNF598 in the regulation of mitophagy is also conserved in human cells. Mitochondrial markers (*e.g.*, TOM20, TIM23, and MTCO2) and mitophagy receptors (*e.g.*, NDP52/CALCOCO2, Optineurin (abbr. as OPTN), and P62/SQSTM1 were degraded faster in HEK293 cells having ectopic expression of ZNF598 and FMRP, compared to control cells, when treated with CCCP (Supplementary Fig. 10h, i). It is noteworthy that ZNF598 and FMRP themselves were also found in mitochondrial fractions and subjected to concurrent degradation through mitophagy.

Next, we wanted to explore the molecular basis by which dZnf598 and Fmr1 regulate mitochondrial biology. First, it was observed that the Fmr1 protein levels were significantly increased in *Usp10* OE flies, despite their divergent effects on mitophagy (Fig. 5g). To elucidate this discrepancy, the tandem co-IP (first round targeting Fmr1-Flag, second round targeting rin) was utilized to investigate the interaction between the Usp10-rin complex and Fmr1. Our result revealed that, i) when *Usp10* is overexpressed, a stable complex is formed between Fmr1 and Usp10-rin; ii) the binding of the Usp10-rin-Fmr1 complex and Hsc70-5 is strengthened under the condition of *Usp10* OE; iii) while, the interaction between the Usp10-rin-Fmr1 complex and porin/VDAC is significantly weakened in the same scenario (Fig. 5h).

Recent research findings suggest that, FMRP binds to VDAC to modulate ERMCS formation and manage the Ca^{2+} influx into the mitochondria[95]. Hence, the competitive binding of USP10-G3BP1 (Usp10-rin in *Drosophila*) complex and porin/VDAC for Fmr1/FMRP causes a local deficiency. The localized shortage of FMRP thus stimulates the formation of ERMCS, effectively preventing the onset of autophagy[96]. In our enhanced CLIP (UV cross-linking and immunoprecipitation) assay of Fmr1, we found that OE of *Fmr1* alone failed to enhance its binding to Hsc70-5 (instead of binding to porin) as *Usp10* OE did. Additionally, co-OE of *Fmr1* and *Usp10* did not further enhance the effect of *Usp10* (Supplementary Fig. 11a), suggesting potential saturation of Fmr1. The results indicated that the combination of *Usp10* RNAi and *Fmr1* OE phenotypically resembled the effects of *Fmr1* OE alone, thereby implying that Usp10 was the primary factor. Consistent with this inference, we found that OE of *Usp10* and *rin*, as well as *Fmr1 RNAi*, increased mitochondrial Ca^{2+} signals. Conversely, suppressing *Usp10* and *rin* had a similar effect to *Fmr1* OE, whereby their mitochondrial Ca^{2+} levels either remained or decreased (Fig. 5i, j, Supplementary Fig. 11b, c). Thus, the role of Fmr1 opposes that of Usp10, explaining why *Fmr1* OE can counteract the effects of *Usp10* OE and result in enlarging mitochondrial size in fly muscles (Fig. 5a). Moreover, even though dZnf598 is an early participant in the RQC pathway, its presence was still detected within the Usp10-rin-Fmr1 complex, exhibiting increased binding affinity to Fmr1 when *Usp10* is overexpressed (Supplementary Fig. 11d). Subsequently, in continuation of our prior study showing the impact of sulfaquinoxaline on mitochondrial fragmentation in *Drosophila* (Fig. s6h, s6i), we examined their interactions upon readthrough-triggered RQC activation. An increase in RQC correlated with a higher binding affinity of the USP10-rin complex, including Fmr1, to the 40S ribosomal subunit (Supplementary Fig. 11e). In short, we demonstrated that Fmr1 and dZnf598 are connected in structure and function to the Usp10/Rin complex to modulate mitochondrial functions (Fig. 5k).

The 40S ribosomal subunit recycling complex is involved in the regulation of ERMCS

The modulation of mitochondrial Ca^{2+} levels by *Usp10* and *rin* suggests their potential capability to influence ERMCS. To test this hypothesis, we first analyzed the genetic interactions between components of ERMCS with Usp10 and Rin. Mitochondrial fragmentation in muscle tissues was markedly attenuated in *Usp10* and *rin* OE flies upon knockdown of certain ERMCS subunits, such as Itpr (the *Drosophila* homolog of human IP3R), porin (the homolog of human VDAC), and MCU (the homolog of human MCU) (Fig. 6a, b). Immunoblot analysis of autophagy (*e.g.*, ref(2)P and Marf) and mitochondrial markers (*e.g.*, mt:CoII, Tom20, and Tim23) revealed that suppression of ERMCS genes effectively prevented the hindrance of mitophagy caused by *Usp10* OE (Supplementary Fig. 12a, b). The hindrance of mitophagy could potentially come from an increase in ERMCS formation, warranting a further look into the regulatory role of Usp10 and rin in ERMCS assembly. The employment of a dual fluorescent organelle labeling system (KDEL-eGFP for the ER; mitoDsRed for mitochondria) in conjunction with 3D reconstruction enabled us to quantify the number of ER-mitochondria tethering sites per mitochondrion in *Drosophila* muscle tissue. Our data indeed demonstrated that both *Usp10* and *rin* OE enhanced ER-mitochondria interactions by promoting tethering (Fig. 6c, d). Furthermore, it was discovered that USP10 and G3BP1 influence ERMCS formation in human cells, with upregulation (of USP10 and G3BP1) leading to an increase and

https://doi.org/10.1038/s41467-025-56346-3

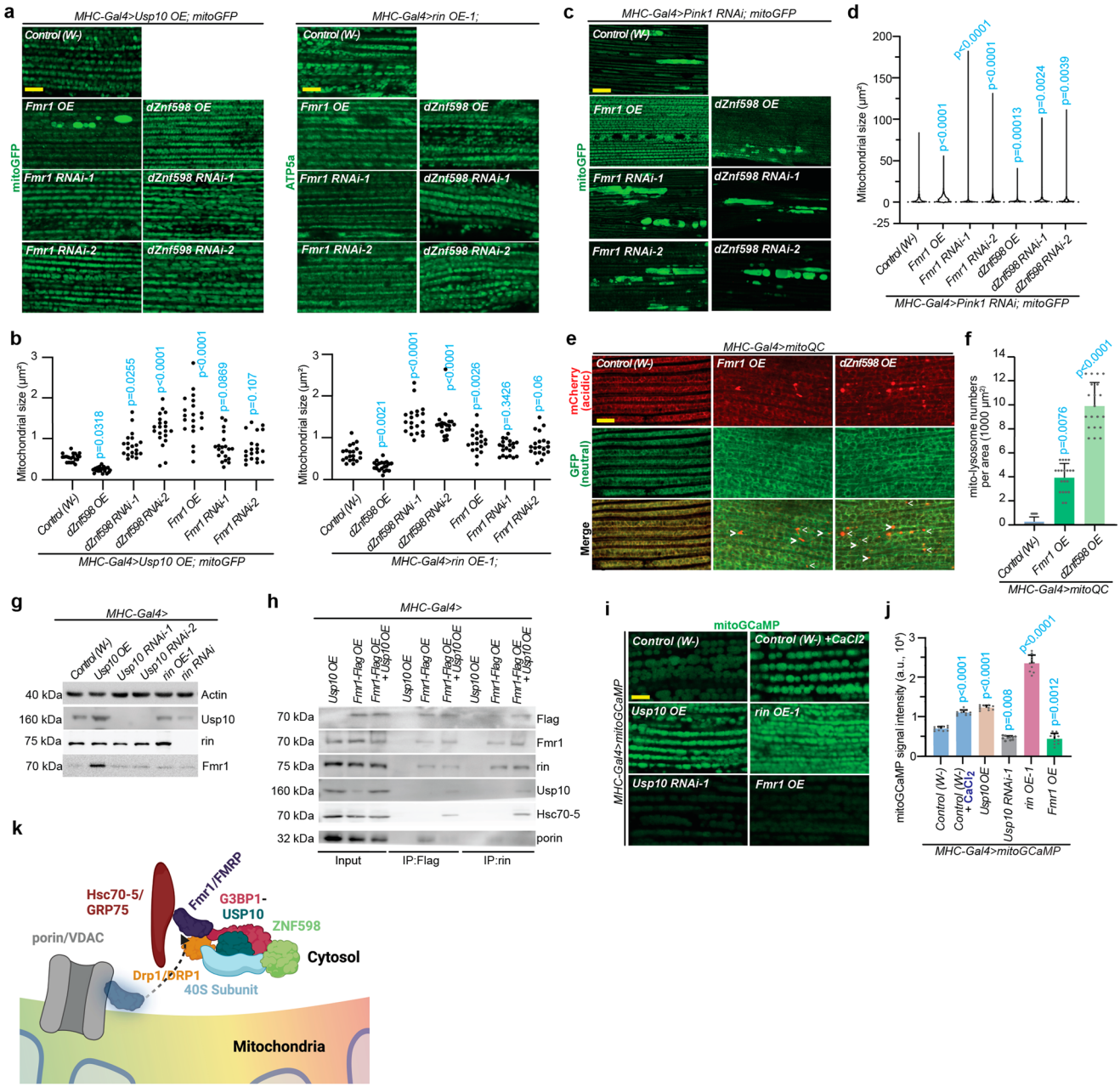

Fig. 5 | dZnf598 and Fmr1 interact with 40S ribosomal subunit recycling complex. a Immunostaining of mitochondrial markers showing the regulation of Fmr1 and dZnf598 in muscle tissue of *Usp10* and *rin* OE flies. Control (*w*-) serves as a negative control. Mitochondrial morphology is visualized by mitoGFP (*Usp10* group) and ATP5α (*rin* group). **b** Quantification of mitochondrial size shown in (**a**). Mitochondria counts were obtained from three samples ($n = 3$, 7 areas counted per sample). **c** Immunostaining showing the effect of Fmr1 and dZnf598 on mitochondrial morphology in muscle tissue of *Pink1 RNAi* flies. Mitochondrial morphology is visualized using mitoGFP. **d** Violin plots showing the quantification of mitochondrial aggregations in (**c**). Significance was calculated using a two-proportion Z test with a threshold set as 3 μm². Three samples ($n = 3$) were analyzed. Statistical parameters are introduced in the Methods section and source code. **e** Mito-lysosome analysis showing increased mitophagy levels promoted by *Fmr1* OE and *dZnf598* OE. Control (*w*-) serves as a negative control. White arrowheads indicate the mito-lysosomes. **f** Quantification of positive mito-lysosomal signals shown in (**e**). An increased mito-lysosome number indicates elevated mitophagy. Twenty replicates were analyzed ($n = 20$). **g** Immunoblotting showing the effect of *Usp10* OE on the Fmr1 protein level. Control (*w*-) serves as a negative control; Actin is used as a loading control in blots. **h** Tandem co-IP analysis using Flag tag (Fmr1) and rin antibodies in sequence, showing the interacting proteins with the Usp10-rin-Fmr1 complex. Three experiments ($n = 3$) were conducted. **i** MitoGCaMP imaging in fly muscle tissue showing the regulation of mitochondrial Ca^{2+} levels by Usp10, rin, and Fmr1. **j** Quantification of images shown in (**i**). Data were obtained from ten samples ($n = 10$). One-way ANOVA test (two-sided) followed by post hoc Dunnett's multiple comparisons test 95% confidence interval (CI) was used in (**b**, **f**, **j**). **k** A working model illustrating the interactions between the 40S ribosomal subunit recycling complex and Fmr1 and dZnf598. The figure was created in BioRender[135]. All scale bars, 5 μm. Data are means ± SEM. The *p* values are included in the figure. Source data are provided as a Source Data file.

downregulation of *USP10* leading to a reduction in the gathering of mitochondria and ER (Supplementary Fig. 12c–e). Notably, *ZNF598/dZnf598*, *NEMF/Clbn* (*Drosophila* homologs) were not observed to contribute to this regulation, indicating that the impact on ERMCS assembly may stem from the 40S ribosomal subunit recycling pathway (Fig. 6c, d, Supplementary Fig. 12c–e).

Subsequently, we asked whether the Usp10-rin complex has a physical interaction with ERMCS. We counterstained the Usp10-rin

https://doi.org/10.1038/s41467-025-56346-3

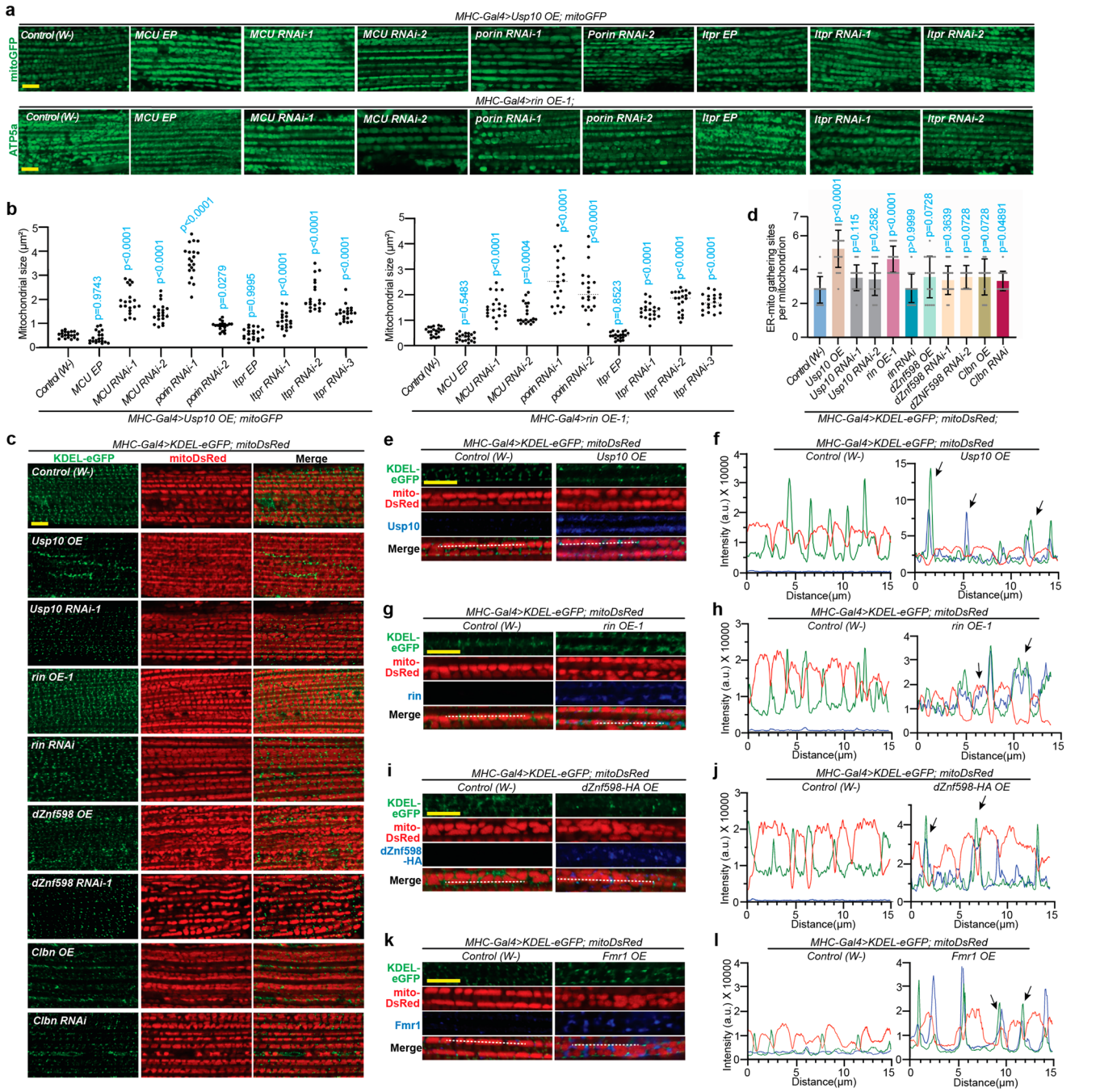

Fig. 6 | The 40S ribosomal subunit recycling complex is associated with ERMCS. **a** Immunostaining of mitochondrial markers showing the regulation of ERMCS genes in muscle tissue of *Usp10* and *rin* OE flies. Control (*w-*) serves as a negative control in each genetic background. Mitochondrial morphology is visualized by mitoGFP in *Usp10* OE, and by ATP5α signal in *rin* OE samples. **b** Quantification of mitochondrial size shown in (**a**). Mitochondria counts were obtained from three samples ($n = 3$, 7 areas counted per sample). **c** Immunostaining of mitoDsRed (a mitochondrial-targeted DeRed reporter) and KDEL-eGFP (An eGFP and KDEL fusion protein, ER marker) showing the regulation of mitochondria-ER gathering by RQC genes in fly muscle tissue. Control (*w-*) serves as a negative control. **d** Quantification of the number of gathering sites per mitochondrion in each genotype shown in (**c**). Gathering site counts were obtained from three samples ($n = 3$, 7 areas counted per sample). One-way ANOVA test (two-sided) followed by post hoc Dunnett's multiple comparisons test 95% confidence interval (CI) was used in (**b, d**, **e**, **g**, **i**, **k**). Immunostaining of mitoDsRed, KDEL, and components of the 40S ribosomal subunit recycling complex, Usp10 (**e**), rin (**g**), dZnf598 (**i**), and Fmr1 (**k**), showing their colocalizations with ERMCSs in fly muscle tissue. Mitochondrial morphology is visualized by mitoDsRed and ER morphology is visualized by KDEL-eGFP. White dashed lines indicate the regions where colocalization analysis was performed in **f**, **h**, **j**, **k**, respectively. Three samples ($n = 3$) were analyzed. **f, h, j, l** Colocalization analyses of images shown in **e, g, i, k**, respectively. Black arrows indicate the colocalization of Usp10 (**e**), rin (**g**), dZnf598 (**i**) and Fmr1 (**k**) with ER signals close to mitochondria. All scale bars, 5 μm. Data are means ± SEM. The *p* values are included in the figure. Source data are provided as a Source Data file.

complex proteins in flies expressing KDEL-eGFP (ER) /mitoDsRed (mitochondria) markers. The proteins Usp10, rin, Fmr1, and dZnf598 were observed to co-localize with the ER region proximal to mitochondria (Fig. 6e–l). Similarly, the proteins USP10, G3BP1, FMRP and ZNF598 were observed to co-localize with ER and mitochondrial signals in NHA cells (Supplementary Fig. 13a, b). Later, we utilized PLA to corroborate interactions between 40S ribosomal recycling factors and ERMCS components. The co-localization of dZnf598 with Hsc70-5/

dGrp75[97], a key ERMCS protein involved in regulating Ca^{2+} transfer between ER and mitochondria, was substantiated (Supplementary Fig. 13c). The presence of additional ERMCS, along with an elevated mitochondrial membrane potential, enhances the influx of ions into the mitochondria, thus aiding in the transfer of Ca^{2+} from ER stores to the mitochondrial matrix[98,99]. This finding aligns with our previous measurement of mitochondrial Ca^{2+} signals regulated by Usp10 and rin in *Drosophila* (Fig. 5i, j, Supplementary Fig. 11b, c).

Ultimately, our findings were validated by administering exogenous calcium $CaCl_2$, calcium chelator BAPTA, IP3R antagonist 2-aminoethoxydiphenyl borate (2-APB), and MCU inhibitor RU-360 to *Usp10* OE flies[57]. While the addition of extra calcium did not produce a notable impact on mitochondrial morphology, reducing calcium uptake by using BAPTA, 2-APB, and RU360, decreased the number of ERMCSs and mitigated mitochondrial fragmentation (Supplementary Fig. 14a–c). It is worth noting that no genetic link appears to exist with ER-phagy genes like *atlastin*[100] and *Rtnl1*[101], despite alterations in the ER structure induced by *Usp10* OE (Supplementary Fig. 14d, e). By integrating genetic, biochemical, and pharmacological evidence, our study concluded that the recycling of the 40S ribosomal subunit at the interface of the mitochondrial and ER involves an active interaction with the ERMCS complex, thereby modulating mitochondrial Ca^{2+} levels (Supplementary Fig. 14f).

The mTORC2 complex functions as a molecular switch in accommodating mitochondrial activity in response to fluctuations in 40S ribosomal subunit recycling

Previous genetic and proteomic analyses have shown that the components of mTOR complexes are entangled with the 40S ribosomal subunit recycling pathway. It was reported that mTORC2-AKT plays a role in regulating energy metabolism in proximity to ERMCS[55]. Therefore, we aimed to study whether the Usp10-rin complex also impacts mitochondrial activity through mTORC2. The activities of mTORC1 and mTORC2 were first studied in *Usp10* and *rin* OE flies. The phosphorylation on P70S6 kinase at Thr398 and on AKT at Ser505 has been extensively used as reliable indicators of mTORC1 and mTORC2 activity, respectively[102,103]. Elevated mTORC1 activity and reduced mTORC2 activity were seen in *Usp10* and *rin* OE flies, as evidenced by the induction of phospho-Thr398-P70S6 kinase and depletion of phospho-Ser505-AKT signals (Fig. 7a). The significance of mTOR signaling in regulating cellular energy supply and metabolism has been widely acknowledged[104]. We also found that in *Usp10* and *rin* OE flies, upregulation of rictor, a key component of the mTOR2 complex, and suppression of *raptor*, a key component of the mTORC1 complex, effectively restored the reduction of ATP, while the opposite regulations further aggravated its deterioration (Fig. 7b). In line with this, our examination of mitochondrial morphology revealed that OE of mTORC2 components (rictor and Sin1) rescued, whereas their RNAi amplified the mitochondrial fragmentation induced by Usp10 and rin expression (Fig. 7c–e). In contrast, raptor (a component of mTORC1) showed the opposite effect (Fig. 7c–e). The genetic interaction of *Usp10* and mTOR genes is also evident in the dynamic stoichiometry of vital proteins, such as ref(2)P, mitochondrial markers (mt:COII, Tom20, Tim23), polyubiquitin, and Fmr1. The alterations induced by *Usp10* OE were effectively counteracted through downregulating mTORC1 activity (using *raptor* RNAi) or enhancing mTORC2 activity (using *rictor* or *Sin1* OE), emphasizing the significance of mTOR pathways in the Usp10-rin-mediated regulation of mitochondrial physiology (Supplementary Fig. 15a).

Next, we sought to ascertain potential physical interactions between mTOR complexes and the Usp10-rin complex. Through tandem co-IP (first round targeting Sin1-Flag, second round targeting rin), we found that Sin1, the mTORC2 core subunit, firmly interacts with Usp10-rin complex and also interacts with Fmr1 and Hsc70-5, a core component of ERMCS, as well as Drp1 and Marf, the fission-fusion proteins (Supplementary Fig. 15b). Whereas another core protein, TOR, did not show interactions with Usp10, rin or Fmr1, indicating certain selectivity in their interactions (Supplementary Fig. 15c, d). Subsequently, we further validated the identified in situ protein-protein interactions using PLA. We found that Sin1 indeed interacts with rin (Fig. 7f, g), dZnf598 (Supplementary Fig. 15e) and Fmr1 (Supplementary Fig. 15f, g). Importantly, the interaction between mTORC2 (indicated by Sin1-Flag) and the Usp10-rin-Fmr1 complex was enhanced by *Usp10* and *rin* OE (Fig. 7f, g, Supplementary Fig. 15f, g). In contrast, there was a decrease in the interaction between mTORC2 (indicated by Sin1-Flag) and ERMCS (indicated by Hsc70-5), suggesting a potential rivalry for mTORC2 between the 40S ribosomal subunit recycling complex and ERMCS (Fig. 7h, i). Impaired mTORC2 adjacent to ERMCSs may result in various mitochondrial abnormalities, such as elevated mitochondrial membrane potential and calcium uptake capacities[55], in alignment with the findings in *Usp10* and *rin* OE.

This regulatory mechanism is also conserved in mammalian cells. The activity of mTORC2, as indicated by phospho-Ser473-AKT, was significantly reduced in cells overexpressing USP10 and G3BP1, while the activity of mTORC1, as indicated by phospho-Thr398-P70S6 kinase, was conversely increased (Supplementary Fig. 15h). Our previous data showed that the activity of USP10 and its interaction with G3BP1 are crucial in facilitating mitochondrial fission (Fig. 1e, f). Likewise, our data here revealed that mutations in USP10 (C424A, F10A) and G3BP1 (F33W) impede their ability to regulate the functions of mTORC1 and mTORC2 (Supplementary Fig. 15i). Additionally, we found that stimulating the upstream RQC pathway also produces comparable changes in mTORC1 and mTORC2 activity assays. A decrease in mTORC2 activity and an increase in mTORC1 activity were clearly observed in human cells expressing a β-globin nonstop mRNA that yields a CAT-tailed protein product[105] (Supplementary Fig. 15j).

Our analysis found that the interaction between Sin1 with Marf and Drp1 was notably enhanced by *Usp10* OE (Fig. 7j–m), indicating a potential involvement of mTORC2 in mediating the assembly of mitochondrial fission and fusion machineries. The enhanced binding of mTORC2 to the Usp10-rin complex in *Usp10* OE flies suggests that mTORC2 may be released from the IP3R-GRP75-VDAC complex as a result of 40S ribosomal subunit recycling activation. In turn, it interacts with Marf to promote the recruitment of Drp1 and facilitate the establishment of mitochondrial fission/fusion hotspots to induce fission[46]. Additionally, we co-expressed USP10 and G3BP1 in HEK 293 cells to investigate their interaction and identify potential binding partners. In accordance with prior findings, the USP10-G3BP1-FMRP complex shows weak binding affinity with RPL7a, ZNF598, PELO, ASCC3, ABCE1, NEMF, and RAPTOR, while exhibiting strong binding affinity with RPS10, MFN1, MFN2, DRP1, and RICTOR (Supplementary Fig. 15k). This suggests that following the initiation of RQC, the 40S ribosomal subunit recycling complex dissociates from the ribosome quality control trigger (RQT) complex and interacts with the mTORC2 complex and mitochondrial fission-fusion machineries to regulate mitochondrial physiology. In summary, it is believed that mTORC2 interacts with the USP10-G3BP1 complex and plays a significant role in governing mitochondrial morphology and function.

Discussion

Protein translation is regarded as a vital biological process in eukaryotic cells, and the ribosome-associated quality control (RQC) mechanism that resolves translational stalling has attracted considerable attention recently[26]. Several studies have examined the cooperation of RQC with other signaling pathways to respond to ribotoxic stress[5–10], yet important pieces of the puzzle remain unsolved. In this study, we found that downstream of RQC, in the 40S ribosomal subunit recycling pathway, USP10 and G3BP1 (homologous to Usp10 and rin in *Drosophila*) influence mitochondrial dynamics and function,

https://doi.org/10.1038/s41467-025-56346-3

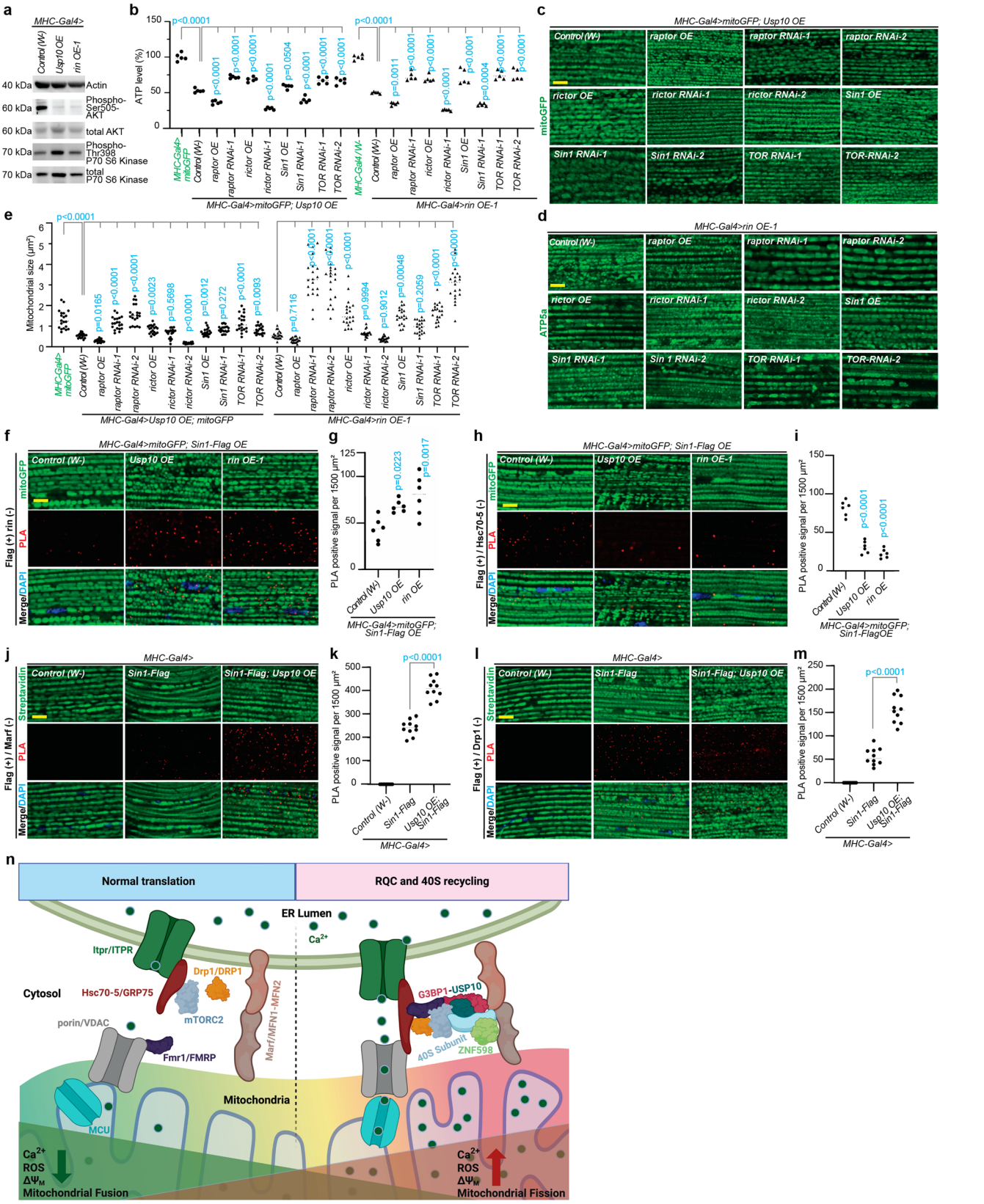

thus reconciling the cellular energy supply from the source. These modulations occur at the ERMCS, acting with the mTORC2 complex, involved in the maintenance of Ca^{2+} homeostasis, the balance of energy metabolism, and remodeling mitochondrial dynamics hotspots (Fig. 7n). Defects in any link in this mechanism ultimately lead to systemic failure of the mitochondrial network and proteome stability, contributing to the onset of the disease. This is evidenced by aberrant protein accumulation and mitochondrial damage in many human diseases, which often coexist and exacerbate each other[106–108].

Upon activation of RQC, mitochondrial fragmentation is observed alongside Ca^{2+} influx, increased mitochondrial membrane potential, and decreased respiratory activity. Why do these phenomena occur

Fig. 7 | The mTORC2 complex interacts with the 40S ribosomal subunit recycling complex. a Immunoblotting showing mTORC1/2 activities in *Usp10* and *rin* OE flies. Control (*w*-) serves as a negative control; Actin is used as a loading control in blots. **b** Standardized ATP measurements (normalized to the Control) on fly muscle samples showing effects of mTOR genes in *Usp10* and *rin* OE flies. 5 male flies were used per group; six independent groups ($n = 6$) were measured per genotype. **c, d** Immunostaining of mitochondrial markers showing the regulation of mTOR genes in *Usp10* OE and *rin* OE flies. Control (*w*-) serves as a negative control. Mitochondrial morphology is visualized by mitoGFP (*Usp10* group) and ATP5α (*rin* group). **e** Quantification of mitochondrial size shown in (**c**, **d**). Mitochondria counts were obtained from three samples ($n = 3$, 7 areas counted per sample). **f** PLA detection of Sin1-Flag(+)/rin(-) interaction (red puncta), showing increased binding in *Usp10* OE and *rin* OE flies. Control (*w*-) serves as a negative control in (**f, h, j, k**). **g** Quantification of images shown in (**f**). **h** PLA detection of Sin1-Flag(+)/Hsc70-5(-) interaction (red puncta), showing decreased binding in *Usp10* OE and *rin* OE flies. **i** Quantification of images shown in **h** Data were obtained from six samples ($n = 6$) in (**g**, **h j**). PLA detection of Sin1-Flag(+)/Marf(-) interaction (red puncta), showing increased binding in *Usp10* OE flies. **k** Quantification of images shown in (**j**). **l** PLA detection of Sin1-Flag(+)/Drp1(-) interaction (red puncta), showing increased binding in *Usp10* OE flies. **m** Quantification of images shown in **l** Data were obtained from ten samples ($n = 10$) in (**k**, **m**). One-way ANOVA test (two-sided) followed by post hoc Dunnett's multiple comparisons test 95% confidence interval (CI) was used in (**b, e**). Two-tailed Student's t-test was used with a 95% confidence interval (CI) in (**g**, **i**, **k**, **m**, **n**). A working model illustrating the interactions between the 40S ribosomal subunit recycling complex, the mTOR pathway, and ERMCS. The figure was created in BioRender[136]. All scale bars, 5 μm. The *p* values are included in the figure. Source data are provided as a Source Data file.

simultaneously? We propose that the effects of RQC on mitochondrial function may be multifaceted. The promotion of the 40S recycling process results in elevated levels of ERMCS assembly, subsequently leading to mitochondrial fragmentation and amplified Ca^{2+} influx[98,99]. The regulation of mitochondrial membrane potential may be attributed to RQC products, particularly CAT-tailed mitochondrial proteins. For instance, a gain of function of the CAT-tail ATP5α protein (a subunit of ATP synthase) would simultaneously cause a reduction in oxidative phosphorylation and an elevation in mitochondrial membrane potential. For further information, please refer to our recent manuscript in *eLife*[109]. Identifying these factors will provide insights into our comprehensive understanding of the cellular quality control network and how dysfunction of the network contributes to the pathogenesis of human diseases.

Another noteworthy observation is the localization of rin. Our data has shown that rin can localize to mitochondria (Supplementary Fig. 4b), which differs from its cytoplasmic distribution in human cells (Fig. 2a). Within the Gene Ontology (GO) terms, *Drosophila* rin-associated mRNAs are enriched in transcription, splicing, and translation, as well as core components of mitochondria[110]. Upon closer examinations of the rin signals depicted in Supplementary Fig. 4b, in flies with *Usp10* or *rin* OE, the rin signal is more localized to mitochondria. On the other hand, despite being orthologs, G3BP1 and rin exhibit divergent functions in their respective systems of mammals and flies. In human cells, OE of G3BPs can induce the formation of stress granules even in the absence of extrinsic stress; whereas in *Drosophila* S2 cells, excessive expression of rin does not induce stress granules formation, highlighting a contrast in their respective functions[111]. This information could facilitate our comprehension of the distinctions among species.

Phosphorylation of eIF2α on serine 51 is also recognized as a dominant biomarker of stress granule assembly[112,113]. Pathological stress granules have been observed in human cells and animal models of several human neurodegenerative diseases, notably Alzheimer's disease, frontotemporal dementia, and C9orf72- or TDP43-related amyotrophic lateral sclerosis[114–116]. Two proteins in our study, G3BP1/rin and FMRP/Fmr1, have been identified as central and ancillary components of stress granules[117–119]. Although OE of G3BP1 has been shown to induce stress granule formation in cultured cells, no such structures were observed in the muscles of *Drosophila*. As outlined earlier, nuclear-encoded mRNAs experience translational arrest and RQC processing in *Drosophila* Parkinson's disease models[13]. However, our findings suggest the absence of predominant stress granule assembly in *Pink1* and *parkin* mutants, indicating the existence of an effective 40S recycling mechanism in these flies. Notably, we cannot rule out the potential involvement of stress granules in the pathogenesis of Parkinson's disease, even with only scattered evidence[120]. In addition, an investigation into the stress granule markers present in dopaminergic neurons is warranted, along with an exploration of the function of Rox8 (the *Drosophila* homolog of human TIA1), to shed light on the fate of defective mRNA molecules under physiological and pathological conditions.

Numerous stress granule components potentially overlap with RQC proteins, including Fmr1/FMRP. A recent study revealed the interaction between FMRP and CNOT1 in regulating RACK1 levels in human and macaque prenatal brains, hinting at its potential role in RQC[121]. In our study, Fmr1 was found to bind with the Usp10-rin complex. The presence of Fmr1 at the ERMCS aligns with the research conducted by Geng et al., indicating an interaction between the C-terminal domain of FMRP and VDAC[95]. However, the precise region of FMRP that interacts with the USP10-G3BP1 complex remains unknown, highlighting the need for further investigation. Further elucidation in biochemical analysis will determine if FMRP undergoes ubiquitination during RQC, and potentially acts as a target for the USP10-G3BP1 complex in subsequent molecular events. We also found that Fmr1 interacts with mTORC2 to jointly regulate mitochondrial function. Fmr1 protein levels showed a substantial increase in *Usp10* overexpressed samples, which may be attributed to heightened protein synthesis or decreased protein degradation resulting from a stable interaction with the Usp10-rin-40S complex. Future examinations of *Fmr1* transcripts and translation efficiency may yield valuable insights.

Another intriguing aspect of Fmr1/FMRP is that, despite the elevated total protein level of Fmr1, the presence of the Usp10-rin-Fmr1/USP10-G3BP1-FMRP complex prevents Fmr1/FMRP from binding to porin/VDAC, resulting in localized depletion at the ERMCS. Thus, akin to *Fmr1 RNAi*, *Usp10* OE rigidifies ERMCS and hinders the occurrence of mitophagy. Nevertheless, the regulation of *Fmr1* expression had a minimal impact on mitochondrial morphology, suggesting that its interaction with the mitochondrial fission-fusion machineries may be contingent upon the presence or activation of the Usp10-rin complex. The mitochondrial fission and fusion machineries co-localize at hotspots of membrane dynamics, allowing for quick responses to changes in mitochondrial metabolism, such as membrane potential[46]. Hence, based on the aforementioned molecular mechanisms, it is hypothesized that the 40S ribosomal subunit recycling complex may initially engage with the ERMCS complex to modulate mitochondrial function and subsequently impact mitochondrial dynamics. Further experimentation is necessary to differentiate the timing of their occurrences.

Finally, in our proteomics analysis, certain proteins were found to have exhibited notable changes in their expression levels. They were not discussed in depth in previous analyses for two reasons: 1) their sporadic occurrence and inability to be categorized in a pathway in GO analysis; 2) their exclusive expression in arthropods, with no orthologs identified in humans. Hence, despite notable changes in their expressions, they are not the primary focus of our study. In *Usp10* OE flies, along with Usp10 itself, increased levels of the proteins Mib2 (mind bomb 2) and Hsp26 (heat shock protein 26). Mib2 is involved in maintaining muscle integrity, while Hsp26 is known to play a role in myosin binding. The changes observed suggest a tendency towards a passive response to damage in muscle tissues, as the muscle damage in

Usp10 OE flies is apparent. The proteins CG15617 (specific to Diptera) and Prm (Paramyosin, a muscle protein found only in invertebrates) showed significantly decreased expression. In *rin* OE flies, the protein CG31087 showed significant upregulation, in addition to rin itself. The CG31087 protein is predicted to activate ecdysteroid 22-kinase activity, which is also exclusive to arthropods. We also found that Lsp2 (larval serum protein 2) was strongly upregulated in both *Usp10* and *rin* OE flies. Lsp2 shows elevated expression in third-instar larvae and pupae, functioning as an amino acid reservoir for adult protein synthesis. This implies a potential connection to the changes in protein expression in adults, despite being a protein unique to metamorphosing insects. Distant homologs of these proteins in mammals may provide insights into the complex role of the USP10-G3BP1 complex, but more extensive and in-depth studies are needed in the future.

Methods

Please refer to Supplementary Table 1: Key Resources Table in the Supplementary Information file.

Cell culture, transfection, knockdown, and drug treatment

HeLa and HEK 293 T cells were cultured in standard conditions (1x DMEM medium, 8.75% fetal bovine serum, 5% CO_2, 37 °C, supplemented with penicillin/streptomycin). GFP-Parkin/HeLa cells were cultured in the same conditions supplemented with 1 μg/mL puromycin as a selective antibiotic marker. HeLa, GFP-Parkin/HeLa, and HEK 293 T cells were transfected with the Invitrogen Lipofectamine 3000 reagent. Gene knockdown experiments were conducted using the Invitrogen Lipofectamine RNAi MAX reagent, following the manufacturer's instructions. The E6/E7/hTERT immortalized Normal Human Astrocyte (NHA) cells were a gift from Dr. Russell O. Pieper at the University of California, San Francisco[60]. NHA cells were cultured under standard conditions (AGM™ Astrocyte Growth Medium Bullet-Kit™), and transfected with the X-tremeGENE™ HP DNA Transfection Reagent.

In the drug treatment experiments conducted in this study, NHA cells were exposed to 20 μM CCCP and Emetine for 4 hours, and 20 μM sulfaquinoxaline (24 hours), followed by an evaluation of alterations in mitochondrial morphology.

Puromycin (Pum) labeling of stalled nascent peptide chains

NHA cells and dissected *Drosophila* muscle samples were pre-incubated with homoharringtonine (5 μM) for 10 minutes, followed by treatment with emetine (100 μM) and puromycin (100 μM) for 15 minutes to label stalled nascent peptides[61]. Protein samples were extracted, assessed using electrophoresis, and subjected to immunoblotting with an anti-puromycin antibody.

Drosophila stocks, fly culture, and drug treatment

All lines were outcrossed six times to a reference background (isogenized *w-* stock) in order to minimize genetic background variations. The resources of Drosophila stocks used in this study are listed in the Supplementary Table 1.

Flies were raised at 25 °C, under a 12/12-hour dark/light cycle, with approximately 65% humidity. Flies were provided with a standard diet (17 L water, 93 g agar, 1716 *g* cornmeal, 310 g brewer's yeast extract, 517 g sucrose, 1033 g dextrose), unless stated otherwise. Fly crosses were performed according to standard procedures. Adult flies were collected after eclosion and assigned into individual vials (~20 flies per vial) for maturation, aging, and waiting for experiments. Vials were flipped every other day.

For drug administration in *Drosophila*, food vials were prepared by mixing instant *Drosophila* medium (1 g dry powder) with Millipore water (5 mL), and supplemented with DMSO (0.1%, vehicle), $CaCl_2$ (10 mM), BAPTA (100 μM), 2-ABP (50 μM) and Ru360 (2 μM), Apigenin (40 μM), thapsigargin (25 μM), Emetine (200 μM), CCCP (40 μM) and Sulfaquinoxaline sodium salt (20 μM). 10 young male flies, within 5 days post-eclosion, were placed into each vial. A total of 4-5 biological replicates (independent vials) were examined per dose per genotype. Vials were flipped every day. Samples were collected for further analysis after 7 days of treatment.

Genetic screening for factors affecting mitochondrial morphology

Usp10 OE in *Drosophila* causes excessive mitochondrial fission in the indirect flight muscles. The purpose of this genetic screen is to identify potent genetic modifiers of *Usp10* using the mitochondrial morphology as a readout. The effects of these modifiers may either enhance or attenuate the effects of *Usp10* OE on mitochondrial dynamics. The UAS-GAL4 system was used to co-express *Usp10* and the modifiers in fly muscles[83], followed by the microscopic analysis of changes in mitochondrial morphology[84]. The screening pool analyzed various pathways that have been implicated in potential genetic interactions with *Usp10*, mitochondrial metabolism, and fission-fusion genes, as well as genes involved in translation regulation and RQC pathways. The results of the screening are summarized in Supplementary Data 2.

Abnormal wing posture and jumping activity analyses

25 male flies were aged at 25 °C for 14 days per vial for wing posture analysis, while 10 male flies were aged at the same conditions for a jumping activity test. The penetrance of abnormal wing posture was determined by calculating the percentage of flies exhibiting either a held-up or drooped wing posture[103]. The analysis of the jumping activity was carried out according to the previously outlined methods[103,122]. For each genotype, a minimum of 3 replicates was assessed in the assays.

Measurement of ATP levels

As described previously, the *Drosophila* thoracic ATP level was measured using a luciferase-based bioluminescence assay (ATP Bioluminescence Assay Kit HS II)[103]. Five thoraces from 7-day-old male flies were dissected for each measurement. Following homogenization of the thoraces in 100 μL of lysis buffer, the specimens were boiled for 5 minutes and then centrifuged at 20,000x *g* for 3 minutes. Afterward, 2.5 μL of the resultant supernatant was diluted using 187.5 μL of dilution buffer and 10 μL luciferase/luciferin mixture provided with the assay kit. The luminescence was promptly measured using a microplate reader (Synergy 2, BioTek, USA). A minimum of 5 independent measurements were carried out for each genotype.

Lifespan assessment

The lifespan test was performed in a manner consistent with the previous method[123], with minor adjustments. Newly hatched flies were collected and randomly divided into different groups. Flies were flipped into vials with fresh food every two days following being counted and recorded. Three groups, each consisting of flies with a specific genotype, were utilized, totaling 75 participants.

Mito-roGFP signal analysis

On day 3 (48 h after eclosion), flies expressing the mito-roGFP2 marker from different genotypes were dissected in Schneider's medium. After dissection, muscle fibers were placed in a mounting medium on a thin cover slip attached to a petri dish. Images were captured using a Zeiss LSM800 confocal microscope with a 510 - 540 emission filter for excitation at 405 and 488 nm. Three independent samples were imaged per group, and three equal-sized images (31.6 μm × 31.6 μm) of muscle area were analyzed. The 405 nm/488 nm fluorescence was obtained using ZEN 3.1 software. ImageJ (NIH) was employed to subtract background and conduct image processing. Measurements were taken from 10 samples for each genotype, across three independent biological replicates.

Mitochondrial morphology and immunohistochemical analysis

Male flies were aged for 7 days at 25 °C prior to tissue collection for the analysis of mitochondrial morphology in the indirect flight muscle and brains. Five independent replicates were dissected for each genotype in the muscle staining. A minimum of seven fly brains were analyzed for each genotype in the dopaminergic neuron staining.

For immunohistochemical examination of mitochondrial morphology, fly thoraces and heads were isolated and fixed in PBSTx (1x PBS, 0.25% Triton X-100) supplemented with 4% formaldehyde. The samples were briefly rinsed, dissected, and then blocked with 5% normal goat serum in 1x PBSTx for 60 minutes at room temperature. The samples were incubated overnight at 4 °C with primary antibodies, which were diluted in the blocking buffer. The primary antibodies used here were rabbit anti-*Drosophila* TH (1:500), mouse anti-ATP5a (1:1000), and chicken anti-GFP (1:1000). Following three 10-minute washing cycles with 1x PBSTx at room temperature, the samples were incubated with fluorophore-conjugated secondary antibodies (1:500) for 3 hours at room temperature in the dark. After undergoing three additional 10-minute washing cycles with 1x PBSTx at room temperature, the samples were mounted onto slides. The slides were subsequently captured using a Zeiss LSM800 Meta confocal microscope and analyzed with the ZEN Blue Edition Software.

When assessing mitochondrial morphology in NHA cells, the mitochondrial population was classified into three distinct phenotypes based on their length: fragmented (<1 μm), tubular (1-3 μm), and elongated (>3 μm)[124]. The determination of mitochondrial phenotype in NHA cells relied on the visual assessment of mitochondria, with a specific focus on more than 70% of the total mitochondrial pool. The assessment was conducted by utilizing designated mitochondrial markers (e.g., Tom20 or mitoDsRed), allowing for the categorization of mitochondria into fragmented, tubular, or elongated/hyperfused groups.

Mito-lysosome analysis using the mitoQC reporter

Following tissue collection, fly thoraces were fixed in PBSTx with 4% formaldehyde for 1 ~ 2 hours at room temperature. Afterward, the samples were dissected and examined directly using a confocal fluorescence microscope (Zeiss). A square area of 31.6 μm × 31.6 μm was set for analyzing the number of mito-lysosomes. A total of 10 samples from three independent biological replicates were counted.

Imaging of mitochondrial calcium level using the mitoGCaMP reporter

The *MHC-Gal4* driver was used to induce the expression of mitoGCaMP (a GCaMP 3.0 protein fused with an N-terminal mitochondrial targeting sequence) in adult flies that were raised at 29 °C. Fly thoraces were dissected in Schneider's medium and promptly placed on the glass slides for living imaging using a Zeiss LSM800 confocal microscope. All imaging parameters that could influence image intensity were maintained consistently throughout all data acquisitions. This encompasses objective lens (e.g., 40x oil-immersion objective, 1x digital zoom), lamp power or laser power (e.g., 488 nm excitation laser with 20% output power, pinhole 1 AU), filter sets or wavelength collections (e.g., GFP filter), acquisition speed (e.g., speed 4), camera or PMT settings, type of mounting media, etc. A square of 31.6 μm × 31.6 μm was designated for the analysis of GCaMP signal intensity. A total of 10 samples from three independent biological replicates were measured for each genotype.

Imaging of mitochondrial superoxide level using MitoSOX™

Following tissue collection, fly thoraces were dissected in Schneider's medium. The muscle fibers were incubated in Schneider's medium supplemented with MitoSOX™ (5 μM). After a 20-minute incubation at 37 °C, the samples were washed twice for 5 minutes each with medium, and then twice for 5 minutes each with pre-warmed PBS buffer in a dark chamber. The samples were promptly placed on the glass slides for live imaging using a Zeiss LSM800 Meta confocal microscope.

All imaging parameters that could influence image intensity were maintained consistently throughout all data acquisitions. The samples were illuminated under the confocal microscope with excitation at 396 nm and emission collected at 610 nm. A square area of 31.6 μm × 31.6 μm was set for the analysis of MitoSOX signal intensity. A total of 10 samples from three independent biological replicates were measured for each genotype.

Imaging of mitochondrial membrane potential using JC-10 dye

Following tissue collection, fly thoraces were dissected in Schneider's medium. The muscle fibers were incubated in Schneider's medium supplemented with JC-10 dye (5 μM) at 37 °C for 30 minutes. The samples were rinsed twice for 5 minutes each with medium and then twice for 5 minutes each with pre-warmed PBS buffer in a dark chamber. The samples were promptly placed on the glass slides for live imaging using a Zeiss LSM800 Meta confocal microscope.

All imaging parameters that could influence image intensity were maintained consistently throughout all data acquisitions. This encompasses objective lens (e.g., 40x oil-immersion objective, 1x digital zoom), lamp power or laser power (e.g., 488 nm excitation laser, 20% output power, pinhole 1 AU), filter sets or wavelength collections (e.g., GFP filter), acquisition speed (e.g., speed 4), camera or PMT settings, type of mounting media, etc. The samples were illuminated under the confocal microscope at 488 nm excitation and emissions between 515/545 nm and 575/625 nm. A square area of 31.6 μm × 31.6 μm was set for the analysis of mitochondrial membrane potential. A total of 10 samples from three independent biological replicates were measured for each genotype.

Imaging of mitochondrial calcium level using the Rhod-2 dye

Following tissue collection, fly thoraces were dissected in Schneider's medium. The muscle fibers were incubated in Schneider's medium supplemented with Rhod-2 dye (5 μM) at 37 °C for 30 minutes. The samples were washed twice for 5 minutes each with medium and twice for 5 minutes each with the pre-warmed PBS buffer in a dark chamber. The samples were promptly placed on the glass slides for live imaging using a Zeiss LSM800 Meta confocal microscope.

All imaging parameters that could influence image intensity were maintained consistently throughout all data acquisitions. This encompasses objective lens (e.g., 40x oil-immersion objective, 1x digital zoom), lamp power or laser power (e.g., 543/561 nm excitation laser, 20% output power, pinhole 1 AU), filter sets or wavelength collections (e.g., GFP filter), acquisition speed (e.g., speed 4), camera or PMT settings, type of mounting media, etc. The samples were illuminated under the confocal microscope at excitation at 557 nm and emissions at 581 nm. A square area of 31.6 μm × 31.6 μm was set for the analysis of mitochondrial calcium signal intensity. A total of 10 samples from three independent biological replicates were measured for each genotype.

Imaging of mitochondria-ER contact sites in Drosophila

The *MHC-Gal4* driver was used to drive the expression of mitoDsRed and KDEL-GFP reporters in flies that were raised at 25 °C. The mitoDsRed and KDEL-GFP reporters were used to label mitochondria and ER, respectively. Fly thoraces were collected and fixed in PBSTx with 4% Formaldehyde for 1 hour. The samples were dissected and examined using a Zeiss LSM800 confocal microscope. Images for 3D acquisition were captured using a 63x oil immersion objective, employing Z-stack imaging to obtain a series of images at a set interval of 0.1 μm with the same x- and y-axis positions. All images were subjected to ZEISS Airy Scanning Mode and the generation of 3-dimensional images using the ZEN Blue Edition Software. The

quantitative analysis of z-stack images was conducted by counting the number of ERMCS per mitochondrion in each genotype within 5 randomly selected squares of 15 µm × 15 µm.

Proximity ligation assay (PLA)

The Duolink® In Situ Red Starter Kit Mouse/Rabbit (Sigma-Aldrich) was utilized for PLA analysis, which contains anti-Rabbit PLUS/anti-Mouse MINUS probes, detection reagents red, wash buffers, and mounting medium with DAPI. The protocol outlined in the Duolink In situ-Fluorescence User Guide was optimized for the requirements of the experiment. The isolated fly thoracic tissues were fixed in PBSTx with 4% formaldehyde. The samples were dissected and subsequently blocked with Duolink® blocking solution, followed by incubation overnight at 4 °C with primary antibodies (see Supplementary Table 1 for details):

- **Anti-HA (1:1000)** for Marf-HA for dZnf598-HA detection
- **Anti-Usp10 (1:1000)** for Usp10 detection
- **Anti-rin (1:1000)** for rin detection
- **Anti-RpS10 (1:1000)** for RpS10 detection
- **Anti-RpL7a (1:1000)** for RpL7a detection
- **Anti-Flag (1:1000)** for Sin1-Flag detection
- **Anti-Hsc70-5 (1:1000)** for Hsc70-5 detection
- **Anti-Drp1 (1:1000)** for Drp1 detection
- **Anti-fmr1 (1:1000)** for Fmr1 detection

Following the Duolink® PLA probe incubation, ligation, amplification, and final wash steps, the samples were then mounted on slides with a DAPI-containing mounting medium as described in the manufacturer's protocol. Alexa Fluor™ 488 streptavidin (**green channel**) was used to visualize mitochondria, while the **PLA signals** were detected in the **red channel** Direct protein interactions (distances <40 nm) were visualized as red fluorescent puncta and imaged with a Zeiss LSM800 confocal microscope. The quantity of PLA puncta per sample was analyzed using ImageJ software.

Mitochondria purification

To purify mitochondria from fly thoraces as previously described[125], dissected samples were homogenized with a Dounce homogenizer in a pre-chilled homogenization buffer solution (HBS buffer: 5 mM HEPES, 70 mM sucrose, 210 mM mannitol, 1 mM EGTA, 1x protease inhibitor cocktail, 0.1 mg/mL cycloheximide, and 1x RNase inhibitor). Following two rounds of centrifugation (1500x *g* and 13,000x *g*), the mitochondria pellets were resuspended and washed twice in the HBS buffer. Subsequently, the samples were resuspended again and loaded on top of pre-made Percoll gradients (15%-22%-50%). The fraction located between the 22% and 50% Percoll gradients, which contained intact mitochondria, was carefully transferred into a new tube. It was then combined with 3 volumes of HBS buffer and subjected to centrifugation at 22,000x *g* for 45 minutes at 4 °C to collect pellets for further analysis.

SDS-PAGE sample preparation, gel preparation, and running conditions

Commercial gels. For SDS-PAGE and immunoblotting analysis, NuPAGE 4-12% Bis-Tris Protein Gels and NuPAGE MOPS SDS running buffer were used.

Home-made gels. The home-made Laemmli resolving gel (per 10 mL) contained 3 mL of 40% Acrylamide/Bis (Bio-Rad), 2.5 mL of 1.5 M Tris-HCl pH 8.8 (Bio-Rad), 1 mL of 10% SDS (Bio-Rad), 50 µL of 10% APS (Bio-Rad) and 5 µL of TEMED (Bio-Rad). The stacking gel (per 2.5 mL) contained 0.25 mL of 40% Acrylamide/Bis, 0.63 mL of 0.5 M Tris-HCl pH 6.8 (Bio-Rad), 250 µL of 10% SDS, 12.5 µL of 10% APS and 2.5 µL of TEMED. The running buffer (per 1 L) contained 3 g Tris base (Sigma-Aldrich), 14.4 g Glycine (Sigma-Aldrich), and 1 g SDS (Sigma-Aldrich).

Blue native gel analysis. Following the purification of mitochondria from samples, the mitochondrial pellets were placed on ice and solubilized in an HBS buffer containing the final 1% Digitonin (Invitrogen) for 30 minutes on ice. The NativePAGE™ Sample Prep Kit (Invitrogen) was used to prepare samples for electrophoresis following the manufacturer's recommended protocol. Samples were run through Blue NativePAGE 3%-12% Bis-Tris Protein Gels using relevant reagents from NativePAGE Running Buffer Kit purchased[126]. The assembly of mitochondrial respiratory chain complexes -I, -V, -II, -III, -IV, and supercomplexes is indicated by the signal intensity of the blue bands at their respective positions.

Immunoblotting. In immunoblotting analysis, *Drosophila* samples from 7-day-old male flies raised at 25°C were used. In each assay, 10 fly thoraces were homogenized in 300 µL lysis buffer (50 mM Tris-HCl pH7.4, 150 mM NaCl, 5 mM EDTA, 10% glycerol, 1% Triton X-100, 0.5 mM DTT, 60 mM β-glycerolphosphate, 1 mM sodium vanadate, 20 mM NaF, and 1x protease inhibitor cocktail). Samples were boiled for 10 minutes, centrifuged at 12,000x *g*, mixed with 4x SDS loading buffer, and separated via the 10% SDS-PAGE. Subsequently, proteins were transferred onto Immobilon P^{SQ} PVDF membranes and hybridized with primary antibodies at 1:1000 dilution overnight at 4°C, followed by incubation with secondary antibodies at 1:10,000 dilution for 2 hours at room temperature. The membranes were incubated with Western Lightning Plus-ECL regent (PerkinElmer) and analyzed using the ChemiDoc Imaging system (Bio-Rad). The primary and secondary antibodies used for immunoblotting are listed in the Supplementary Table 1.

Co-immunoprecipitation (co-IP), tandem co-IP and CLIP assay. In *Drosophila* co-IP experiments, 30 fly thoraces per replicate per genotype were homogenized using a motor homogenizer in pre-chilled lysis buffer supplemented with 0.1 mg/mL cycloheximide and 1x RNase inhibitor. After UV-crosslinking of tissue lysates (see set-up below) and centrifugation at 1500x g for 5 minutes at 4°C, supernatants were either diluted with 2x SDS sample buffer (1:1 ratio) as inputs or processed for immunoprecipitation. Samples for co-IP were first diluted to 1 µg/uL of final protein concentration, then incubated with the indicated antibodies at an optimized amount and 20 uL protein A/G magnetic beads overnight at 4°C. The beads were retrieved using a magnetic stand and washed 3 times 10 minutes each with the pre-chilled lysis buffer. The immunocomplexes in samples were mixed with 2x SDS sample buffer (1:1 ratio), boiled along with input samples for 10 minutes, and subjected to SDS-PAGE and immunoblotting analysis. In human cell co-IP experiments, the cells were first washed with pre-chilled 1x PBS and then crosslinked using a Stratalinker UV crosslinker 2000 at the energy level of 400,000 µJ. Following crosslinking, the cells were incubated for 15 minutes on ice in a cell lysis buffer containing 0.1 mg/mL cycloheximide and 1x RNase inhibitor. Cell lysates were harvested and centrifuged at 1500x *g* for 5 minutes, followed by co-IP application as outlined previously.

In tandem co-IP experiments, samples for the first step of co-IP were first diluted to a final protein concentration of 1 µg/µL, then incubated with 50 µL anti-Flag or anti-HA magnetic beads overnight at 4°C. The beads were retrieved using the magnetic stand and washed 3 times 10 minutes each with the pre-chilled lysis buffer. Samples were incubated in 200 µL elution buffer containing a high concentration (250 mg/mL) of 3xFlag or 3xHA peptide at 4 °C for 6 hours. Supernatants were either diluted with 2x SDS sample buffer (1:1 ratio) as the second input or subjected to the second step of co-IP. The samples for co-IP were incubated together with the indicated antibodies at an optimized amount and 20 µL protein A/G magnetic beads overnight at 4°C. The beads were harvested using the magnetic stand and washed 3 times 10 minutes each with the pre-chilled lysis buffer. Afterward, the immunocomplexes in samples were mixed with 2x SDS sample buffer

(1:1 ratio), boiled along with input samples for 10 minutes, and subjected to SDS-PAGE and immunoblotting analysis.

Colocalization analysis in human cells. To measure the pixel intensity-based colocalization, the colocalization tool of ZEN software was used. Colocalization analysis was performed on a pixel-by-pixel basis. All imaging parameters that can influence the image intensity were kept constant for all data acquisition. This included objective lens, lamp power or laser power, filter set or wavelength collection, acquisition speed, camera or PMT settings, mounting media type, etc. Colocalization coefficients between TOM20 and KDEL-eGFP were calculated with the ZEN software on LSM800 by randomly selecting and analyzing seven imaged fields, including a minimum of 7 cells in each field. Mander's overlap coefficients (MOC) were calculated to measure the colocalization of proteins based on total number of pixels per protein as follows[127]:

$$M1 = \frac{red \cap green}{red} and M2 = \frac{red \cap green}{green}$$

Two-proportion Z test. The mitochondrial area (indicated by mitoGFP) was first measured using ImageJ software as described before[128]. The resultant data were subjected to the two-proportion Z test to compare two experimental proportions. This study has used the two-proportion Z test to specify whether the percentages of values above a certain threshold significantly differ between the experimental and control groups. The null and alternative hypotheses of this test are as follows:

$$H_0 : p_e - p_c = 0; H_1 : p_e - p_c \neq 0$$

In this equation, p_c *and* p_e are the proportion of values higher than the pre-specified threshold in the control and experimental groups, respectively. The null hypothesis is that the proportions are the same in the control and experimental groups. The alternative hypothesis is that these proportions differ significantly. The test statistic (Z-score) is as follows:

$$Z = \frac{\hat{p}_e - \hat{p}_c}{\sqrt{\hat{p}_0(1-\hat{p}_0)\left(\frac{1}{n_e} + \frac{1}{n_c}\right)}}$$

In this equation, $\hat{p}_0$ is defined as the total proportion which is considered as a portion of observed values higher than the threshold between the control and experimental groups. n_c is the sample size in the control group and n_e are the size of the sample in the experimental group. In this study, all *p*-values are calculated with the corresponding test statistic in which the z-score follows a standard normal distribution under the null hypothesis.

Transmission electron microscopy. For TEM analysis, adult male flies around 7 days old, housed at 25°C, were used. Prior to tissue dissection, flies were fed with 5% sucrose and 100 µM cycloheximide for 1 hour at 25°C. Specimens (fly thoraxes) were dissected and fixed in a fixation buffer (2% glutaraldehyde, 4% poly-formaldehyde, 0.6% picric acid in 0.1 M sodium cacodylate buffer, 0.1 mg/mL cycloheximide, pH 7.4) for 1 hour at 25°C. The samples were further sectioned and prepared for TEM analysis by the Electron Microscopy Core Facility at UT Southwestern Medical Center. Images were acquired using a JEOL JEM-1400 transmission electron microscope.

Proteomic analysis and data processing. The UT Southwestern Proteomics Core and Stanford University conducted the sample preparation and subsequent Tandem Mass Tag (TMT) quantification on the Orbitrap Fusion Lumos mass-spectrometry platforms (LC-MS/MS). Fly thoraces were collected and homogenized in the pre-chilled lysis buffer supplemented with 1x proteasome inhibitor cocktail. Tissue lysates were briefly centrifuged to remove cuticle debris and mixed with an equal volume of 10% SDS in 100 mM TEAB (Sigma). Following disulfide bond reduction and alkylation, samples were digested overnight with trypsin using an S-Trap (Protifi). The peptide eluate from the S-Trap was dried and reconstituted in 100 mM TEAB buffer. The TMTpro16-plex Isobaric Mass Tagging Kit (Thermo) was used to label the samples as per the manufacturer's instructions. Samples were split into 2 batches of TMTpro16plex, with A2, F3, G3, H1, and I1 included in both to allow for comparison across the 2 batches. Each batch was cleaned up and fractionated using a Pierce High pH Reversed-Phase Peptide Fractionation Kit (Thermo) into 8 fractions. The fractions were dried in a SpeedVac and reconstituted in a 2% acetonitrile, 0.1% TFA buffer, and diluted such that ~1 ug of peptides were injected for each fraction.

Peptides were analyzed on an Orbitrap Eclipse MS system (Thermo) coupled to an Ultimate 3000 RSLC-Nano liquid chromatography system (Thermo). Samples were injected onto a 75 um i.d., 75-cm long EasySpray column (Thermo) and eluted with a gradient from 0–28% buffer B over 180 min at a flow rate of 250 nL/min. Buffer A contained 2% (v/v) ACN and 0.1% formic acid in water, and buffer B contained 80% (v/v) ACN, 10% (v/v) trifluoroethanol, and 0.1% formic acid in water. at a flow rate of 250 nl/min. Spectra were continuously acquired in a data-dependent manner throughout the gradient, acquiring a full scan in the Orbitrap (at 120,000 resolution with a standard AGC target) followed by MS/MS scans on the most abundant ions in 2.5 s in the ion trap (turbo scan type with an intensity threshold of 5000, CID collision energy of 35%, standard AGC target, maximum injection time of 35 ms and isolation width of 0.7 m/z). Charge states from 2–6 were included. Dynamic exclusion was enabled with a repeat count of 1, an exclusion duration of 25 s and an exclusion mass width of ± 10 ppm. Real-time search was used for selection of peaks for SPS-MS3 analysis, with searched performed against a list of mouse mitochondrial proteins from UniProt along with additional mouse mitochondrial proteins. Up to 2 missed tryptic cleavage was allowed, with carbamidomethylation (+57.0215) of cysteine and TMTpro reagent (+304.2071) of lysine and peptide N-termini used as static modifications and oxidation (+15.9949) of methionine used as a variable modification. MS3 data were collected for up to 10 MS2 peaks which matched to fragments from the real-time peptide search identification, in the Orbitrap at a resolution of 50,000, HCD collision energy of 65% and a scan range of 100 - 500.

Protein identification and quantification were done using Proteome Discoverer v.3.0 SP1 (Thermo). Raw MS data files were analyzed against the *Drosophila* melanogaster-reviewed protein database from UniProt. Both Comet and SequestHT with INFERYS Rescoring were used, with carbamidomethylation (+57.0215) of cysteine and TMTpro reagent (+304.2071) of lysine and peptide N-termini used as static modifications and oxidation (+15.9949) of methionine used as a variable modification. Reporter ion intensities were reported, with further normalization performed by using the total intensity in each channel to correct discrepancies in sample amount in each channel. The false-discovery rate (FDR) cutoff was 1% for all peptides. The proteomic analysis was conducted using R version 4.1.2. The complete dataset was standardized, and batch effects were removed by Combat from the sva package[129,130]. The principal component analysis (PCA) was conducted using the factoextra package, which can reduce the dimensionality of the data without losing important information, to check whether the different groups could be separated sufficiently to test the effect of batch effect correction. Relative fold changes in protein expression and statistical significance in genotypes were calculated with Limma[131]. The Limma package (Linear Models for Microarray Data) fits a linear model for each gene and uses an empirical Bayes approach to adjust for gene variance. It uses null hypothesis testing, which is two-sided by default. For our sample, it has 2 groups with 3 replicates each and a residual degree of freedom (df) of 4.

Confidence intervals (CI) are set to 95% as shown in the table. Effect sizes are expressed as log2(FC). For each genotype (OE and RNAi), we visualized log fold change and false discovery rate (FDR) using symmetric volcano plots using ggplot2 package[132], showing selected thresholds for statistical significance (FDR < 0.05) and normalized ratios (| log2(FC)| > 0.323). The threshold (log2(FC) = 0.323) was chosen to capture small yet potentially important biological variations, especially within the scope of our specific study objectives. The choice of differential expression threshold is contingent upon the study design, biological background, and research objectives. Our selection was made based on the thresholds used in similar studies, highlighting the importance of subtle changes in the biological process being studied[89–91]. Next, differentially expressed proteins in each genotype compared to the control group were subjected to a network-based analysis to highlight molecular pathways affected by *Usp10* and *rin*. To construct this protein-protein interaction (PPI) network, we utilized the gene set enrichment analysis (GSEA, GSEA v4.2.3)[92]. GSEA uses a permutation test to calculate whether the enrichment score is significant. We used 1000 permutations in the enrichment analysis, and gene sets with FDR < 0.05 were considered significant. We used Reactome as the pathway database for *Drosophila*[133]. Each genotype was paired with the control group, and each pair, after being ranked according to differential expression, was compared against the pathways in Reactome. An enrichment score and FDR were calculated for each comparison. Several pathways with FDR < 0.05 were identified in each genotype.

Statistics and reproducibility

This study's replicates/samples/groups/experiments were biologically independent. Representative images of immunoblots, TEM analysis, blue native gels, and mitochondria analyses in *Drosophila* muscle or brain tissues were independently repeated at least three times. Immunofluorescence staining in fly brains, muscle tissues, and human cells was randomly selected for analysis and repeated at least three times independently unless otherwise stated in figure captions. Please find the "n" numbers in the figure legends. The above description is for one round of independent experiments, and the experimental results shown were repeated at least two times (rounds) at different times to ensure that the results are similar. No statistical method was used to predetermine the sample size. No data were excluded from the analyses due to biological reasons. Samples were randomly allocated into experimental groups. The investigators were not blinded to allocation during experiments and outcome assessment.

All analyses in this study were done using GraphPad Prism 9.4.1 software, except for the two-proportion Z test, which was carried out using R (v4.1.1) (Fig. 5d, Supplementary Figs. 2b, 3f). For pairwise comparisons (Figs. 2e, g, i, k, o, 7k, m, Supplementary Fig. 6b, d), a two-tailed Student's t-test was used with a 95% confidence interval (CI). All data are presented as mean values ± SEM (Standard Error of the Mean). In the case of multiple groups comparisons, we used a one-way ANOVA test followed by post hoc Dunnett's multiple comparisons tests Figs. 1b, h, 2b, c, 3a, b, f, h, 5b, d, f, j, 6b, d, 7b, e, g, i, Supplementary Figs. 1e, 1g, 3c, 3d, 5d, 5e, 5g, 5h, 6i, 6q, 7e, 7g, 10a, 10b, 10e, 11c, 12d, 12e, 14b,14c, s14e, 15g), and two-way ANOVA test (Fig. 1d, 1f, Supplementary Figs. 2d, 6k, 12b). For lifespan analyses, Log-rank (Mantel-Cox) test was carried out (Supplementary Fig. 1a, b).

The *p* values are indicated in the figures. Sample size/statistical details were mentioned separately in the figure legends. In all statistical analyses, a *p*-value less than 0.05 was considered significant unless otherwise stated in the figure legends.

Reporting summary

Further information on research design is available in the Nature Portfolio Reporting Summary linked to this article.

Data availability

All source data (raw images and statistics) used and reported in this study are provided in the Source Data file. The raw data of proteomic datasets is available in the MassIVE repository with accession code MSV000096824. Source data are provided with this paper.

Code availability

The original code for proteomic analysis and two-proportion Z-test can be accessible on GitHub [https://github.com/boxiangliulab/mitochondrial_QC].

References

1. Hipp, M. S., Kasturi, P. & Hartl, F. U. The proteostasis network and its decline in ageing. *Nat. Rev. Mol. cell Biol.* **20**, 421–435 (2019).
2. Brandman, O. & Hegde, R. S. Ribosome-associated protein quality control. *Nat. Struct. Mol. Biol.* **23**, 7–15 (2016).
3. Joazeiro, C. A. P. Mechanisms and functions of ribosome-associated protein quality control. *Nat. Rev. Mol. cell Biol.* **20**, 368–383 (2019).
4. Ikeuchi, K., Izawa, T. & Inada, T. Recent progress on the molecular mechanism of quality controls induced by ribosome stalling. *Front. Genet.* **9**, 743 (2019).
5. Sinha, N. K. et al. EDF1 coordinates cellular responses to ribosome collisions. *eLife* **9**, e58828 (2020).
6. Vind, A. C. et al. ZAKα recognizes stalled ribosomes through partially redundant sensor domains. *Mol. cell* **78**, 700–713.e7 (2020).
7. Yan, L. L. & Zaher, H. S. Ribosome quality control antagonizes the activation of the integrated stress response on colliding ribosomes. *Mol. cell* **81**, 614–628.e4 (2021).
8. Wu, C. C., Peterson, A., Zinshteyn, B., Regot, S. & Green, R. Ribosome collisions trigger general stress responses to regulate cell fate. *Cell* **182**, 404–416.e14 (2020).
9. Wan, L. et al. Translation stress and collided ribosomes are co-activators of cGAS. *Mol. cell* **81**, 2808–2822.e10 (2021).
10. Snieckute, G. et al. Ribosome stalling is a signal for metabolic regulation by the ribotoxic stress response. *Cell Metab.* **34**, 2036–2046.e8 (2022).
11. Kafri, M., Metzl-Raz, E., Jona, G. & Barkai, N. The cost of protein production. *Cell Rep.* **14**, 22–31 (2016).
12. Rolfe, D. F. & Brown, G. C. Cellular energy utilization and molecular origin of standard metabolic rate in mammals. *Physiological Rev.* **77**, 731–758 (1997).
13. Wu, Z. et al. MISTERMINATE mechanistically links mitochondrial dysfunction with proteostasis failure. *Mol. cell* **75**, 835–848.e8 (2019).
14. Su, T. et al. Structure and function of Vms1 and Arb1 in RQC and mitochondrial proteome homeostasis. *Nature* **570**, 538–542 (2019).
15. Izawa, T., Park, S. H., Zhao, L., Hartl, F. U. & Neupert, W. Cytosolic protein Vms1 links ribosome quality control to mitochondrial and cellular homeostasis. *Cell* **171**, 890–903.e18 (2017).
16. Verma, R. et al. Vms1 and ANKZF1 peptidyl-tRNA hydrolases release nascent chains from stalled ribosomes. *Nature* **557**, 446–451 (2018).
17. Matsuo, Y. & Inada, T. The ribosome collision sensor Hel2 functions as preventive quality control in the secretory pathway. *Cell Rep.* **34**, 108877 (2021).
18. Juszkiewicz, S. et al. ZNF598 is a quality control sensor of collided ribosomes. *Mol. cell* **72**, 469–481.e7 (2018).
19. Simms, C. L., Yan, L. L. & Zaher, H. S. Ribosome collision is critical for quality control during no-go decay. *Mol. cell* **68**, 361–373.e5 (2017).

20. Ikeuchi, K. et al. Collided ribosomes form a unique structural interface to induce Hel2-driven quality control pathways. *The EMBO journal* **38**, e100276 (2019).
21. Sundaramoorthy, E. et al. ZNF598 and RACK1 regulate mammalian ribosome-associated quality control function by mediating regulatory 40s ribosomal ubiquitylation. *Mol. cell* **65**, 751–760.e4 (2017).
22. Garzia, A., Meyer, C. & Tuschl, T. The E3 ubiquitin ligase RNF10 modifies 40S ribosomal subunits of ribosomes compromised in translation. *Cell Rep.* **36**, 109468 (2021).
23. Hashimoto, S., Sugiyama, T., Yamazaki, R., Nobuta, R. & Inada, T. Identification of a novel trigger complex that facilitates ribosome-associated quality control in mammalian cells. *Sci. Rep.* **10**, 3422 (2020).
24. Juszkiewicz, S., Speldewinde, S. H., Wan, L., Svejstrup, J. Q. & Hegde, R. S. The ASC-1 complex disassembles collided ribosomes. *Mol. cell* **79**, 603–614.e8 (2020).
25. Shao, S., von der Malsburg, K. & Hegde, R. S. Listerin-dependent nascent protein ubiquitination relies on ribosome subunit dissociation. *Mol. cell* **50**, 637–648 (2013).
26. Shen, P. S. et al. Protein synthesis. Rqc2p and 60S ribosomal subunits mediate mRNA-independent elongation of nascent chains. *Sci. (N. Y., NY)* **347**, 75–78 (2015).
27. Meyer, C., Garzia, A., Morozov, P., Molina, H. & Tuschl, T. The G3BP1-family-USP10 deubiquitinase complex rescues ubiquitinated 40s subunits of ribosomes stalled in translation from lysosomal degradation. *Mol. cell* **77**, 1193–1205.e5 (2020).
28. Kostova, K. K. et al. CAT-tailing as a fail-safe mechanism for efficient degradation of stalled nascent polypeptides. *Sci. (N. Y., NY)* **357**, 414–417 (2017).
29. Li, S. et al. Quality-control mechanisms targeting translationally stalled and C-terminally extended poly(GR) associated with ALS/FTD. *Proc. Natl Acad. Sci. USA* **117**, 25104–25115 (2020).
30. Tourrière, H. et al. RasGAP-associated endoribonuclease G3Bp: selective RNA degradation and phosphorylation-dependent localization. *Mol. Cell. Biol.* **21**, 7747–7760 (2001).
31. Hinton, S. D., Myers, M. P., Roggero, V. R., Allison, L. A. & Tonks, N. K. The pseudophosphatase MK-STYX interacts with G3BP and decreases stress granule formation. *Biochemical J.* **427**, 349–357 (2010).
32. Buchan, J. R. & Parker, R. Eukaryotic stress granules: the ins and outs of translation. *Mol. cell* **36**, 932–941 (2009).
33. Matsuki, H. et al. Both G3BP1 and G3BP2 contribute to stress granule formation. *Genes Cells.: devoted Mol. Cell. mechanisms* **18**, 135–146 (2013).
34. Kedersha, N. et al. G3BP-Caprin1-USP10 complexes mediate stress granule condensation and associate with 40S subunits. *J. cell Biol.* **212**, 845–860 (2016).
35. Aguilera-Gomez, A. et al. Phospho-rasputin stabilization by sec16 is required for stress granule formation upon amino acid starvation. *Cell Rep.* **20**, 935–948 (2017).
36. Kim J. Y. et al. RNAi screening-based identification of usp10 as a novel regulator of Paraptosis. *Scientific reports* **9**, 3175 (2019).
37. Gao, Y. et al. Usp10 modulates the hippo pathway by deubiquitinating and stabilizing the transcriptional coactivator yorkie. *Int. J. Mol. Sci.* **20**, 6013 (2019).
38. Jia, R. & Bonifacino, J. S. The ubiquitin isopeptidase USP10 deubiquitinates LC3B to increase LC3B levels and autophagic activity. *J. Biol. Chem.* **296**, 100405 (2021).
39. Takahashi, M. et al. USP10 is a driver of ubiquitinated protein aggregation and aggresome formation to inhibit apoptosis. *iScience* **9**, 433–450 (2018).
40. Deng, M. et al. Deubiquitination and activation of AMPK by USP10. *Mol. cell* **61**, 614–624 (2016).
41. Soncini, C., Berdo, I. & Draetta, G. Ras-GAP SH3 domain binding protein (G3BP) is a modulator of USP10, a novel human ubiquitin specific protease. *Oncogene* **20**, 3869–3879 (2001).
42. Sowa, M. E., Bennett, E. J., Gygi, S. P. & Harper, J. W. Defining the human deubiquitinating enzyme interaction landscape. *Cell* **138**, 389–403 (2009).
43. Roca-Portoles, A. & Tait, S. W. G. Mitochondrial quality control: from molecule to organelle. *Cell. Mol. life Sci.: CMLS* **78**, 3853–3866 (2021).
44. Hamasaki, M. et al. Autophagosomes form at ER-mitochondria contact sites. *Nature* **495**, 389–393 (2013).
45. Friedman, J. R. et al. ER tubules mark sites of mitochondrial division. *Sci. (N. Y., NY)* **334**, 358–362 (2011).
46. Abrisch, R. G., Gumbin, S. C., Wisniewski, B. T., Lackner, L. L. & Voeltz, G. K. Fission and fusion machineries converge at ER contact sites to regulate mitochondrial morphology. *J. Cell Biol.* **219**, e201911122 (2020).
47. Phillips, M. J. & Voeltz, G. K. Structure and function of ER membrane contact sites with other organelles. *Nat. Rev. Mol. cell Biol.* **17**, 69–82 (2016).
48. Giamogante, F., Barazzuol, L., Brini, M. & Calì, T. ER-mitochondria contact sites reporters: strengths and weaknesses of the available approaches. *Int. J. Mol. Sci.* **21**, 8157 (2020).
49. de Brito, O. M. & Scorrano, L. Mitofusin 2 tethers endoplasmic reticulum to mitochondria. *Nature* **456**, 605–610 (2008).
50. Szabadkai, G. et al. Chaperone-mediated coupling of endoplasmic reticulum and mitochondrial Ca2+ channels. *J. cell Biol.* **175**, 901–911 (2006).
51. Xu, H. et al. IP 3 R-Grp75-VDAC1-MCU calcium regulation axis antagonists protect podocytes from apoptosis and decrease proteinuria in an Adriamycin nephropathy rat model. *BMC Nephrol.* **19**, 140 (2018).
52. Vance, J. E. Phospholipid synthesis in a membrane fraction associated with mitochondria. *J. Biol. Chem.* **265**, 7248–7256 (1990).
53. Zhou, R., Yazdi, A. S., Menu, P. & Tschopp, J. A role for mitochondria in NLRP3 inflammasome activation. *Nature* **469**, 221–225 (2011).
54. Bantug, G. R. et al. Mitochondria-endoplasmic reticulum contact sites function as immunometabolic hubs that orchestrate the rapid recall response of memory CD8 + T cells. *Immunity* **48**, 542–555.e6 (2018).
55. Betz, C. et al. Feature Article: mTOR complex 2-Akt signaling at mitochondria-associated endoplasmic reticulum membranes (MAM) regulates mitochondrial physiology. *Proc. Natl Acad. Sci. USA* **110**, 12526–12534 (2013).
56. Marchi, S. et al. Oncogenic and oncosuppressive signal transduction at mitochondria-associated endoplasmic reticulum membranes. *Mol. Cell. Oncol.* **1**, 956469 (2014).
57. Lee, K. S. et al. Altered ER-mitochondria contact impacts mitochondria calcium homeostasis and contributes to neurodegeneration in vivo in disease models. *Proc. Natl Acad. Sci. USA* **115**, 8844 (2018).
58. Rieusset, J. Contribution of mitochondria and endoplasmic reticulum dysfunction in insulin resistance: Distinct or interrelated roles? *Diab. Metab.* **41**, 358–368 (2015).
59. Paillusson, S. et al. There's something wrong with my mam; the er-mitochondria axis and neurodegenerative diseases. *Trends Neurosci.* **39**, 146–157 (2016).
60. Sapkota, D. et al. Aqp4 stop codon readthrough facilitates amyloid-β clearance from the brain. *Brain: a J. Neurol.* **145**, 2982–2990 (2022).
61. Wu, Z. et al. Ubiquitination of ABCE1 by NOT4 in response to mitochondrial damage links co-translational quality control to PINK1-directed mitophagy. *Cell Metab.* **28**, 130–144.e7 (2018).

62. Yang, Y. et al. Pink1 regulates mitochondrial dynamics through interaction with the fission/fusion machinery. *Proc. Natl Acad. Sci. USA* **105**, 7070–7075 (2008).
63. Ma, P., Yun, J., Deng, H. & Guo, M. Atg1-mediated autophagy suppresses tissue degeneration in pink1/parkin mutants by promoting mitochondrial fission in Drosophila. *Mol. Biol. cell* **29**, 3082–3092 (2018).
64. Piatnitskaia, S. et al. USP10 is a critical factor for Tau-positive stress granule formation in neuronal cells. *Sci. Rep.* **9**, 10591 (2019).
65. Yang, P. et al. G3BP1 is a tunable switch that triggers phase separation to assemble stress granules. *Cell* **181**, 325–345.e28 (2020).
66. Gareau, C. et al. Characterization of fragile X mental retardation protein recruitment and dynamics in Drosophila stress granules. *PloS one* **8**, e55342 (2013).
67. Brand, S. & Bourbon, H. M. The developmentally-regulated Drosophila gene rox8 encodes an RRM-type RNA binding protein structurally related to human TIA-1-type nucleolysins. *Nucleic acids Res.* **21**, 3699–3704 (1993).
68. Alam, M. S. Proximity ligation assay (PLA). *Curr. Protoc. Immunol.* **123**, 58 (2018).
69. Chen, P. L. et al. Vesicular transport mediates the uptake of cytoplasmic proteins into mitochondria in Drosophila melanogaster. *Nat. Commun.* **11**, 2592 (2020).
70. Osuna, B. A., Howard, C. J., Kc S., Frost, A. & Weinberg, D. E. In vitro analysis of RQC activities provides insights into the mechanism and function of CAT tailing. *eLife* **6**, e27949 (2017).
71. Sciuto, M. R. et al. Two-step coimmunoprecipitation (TIP) enables efficient and highly selective isolation of native protein complexes. *Mol. Cell. Proteom.: MCP* **17**, 993–1009 (2018).
72. Clark, I. E. et al. Drosophila pink1 is required for mitochondrial function and interacts genetically with parkin. *Nature* **441**, 1162–1166 (2006).
73. Park, J. et al. Mitochondrial dysfunction in Drosophila PINK1 mutants is complemented by parkin. *Nature* **441**, 1157–1161 (2006).
74. Li, S. et al. Altered MICOS morphology and mitochondrial ion homeostasis contribute to poly(gr) toxicity associated with C9-ALS/FTD. *Cell Rep.* **32**, 107989 (2020).
75. Liu, Z., Celotto, A. M., Romero, G., Wipf, P. & Palladino, M. J. Genetically encoded redox sensor identifies the role of ROS in degenerative and mitochondrial disease pathogenesis. *Neurobiol. Dis.* **45**, 362–368 (2012).
76. Robinson, K. M. et al. Selective fluorescent imaging of superoxide in vivo using ethidium-based probes. *Proc. Natl Acad. Sci. USA* **103**, 15038–15043 (2006).
77. Younes, N. et al. JC-10 probe as a novel method for analyzing the mitochondrial membrane potential and cell stress in whole zebrafish embryos. *Toxicol. Res.* **11**, 77–87 (2021).
78. Yang, Y. et al. Mitochondrial pathology and muscle and dopaminergic neuron degeneration caused by inactivation of Drosophila Pink1 is rescued by Parkin. *Proc. Natl Acad. Sci. USA* **103**, 10793–10798 (2006).
79. Lee, J. J. et al. Basal mitophagy is widespread in Drosophila but minimally affected by loss of Pink1 or parkin. *J. Cell Biol.* **217**, 1613–1622 (2018).
80. Wyant, G. A. et al. NUFIP1 is a ribosome receptor for starvation-induced ribophagy. *Sci. (N. Y., NY)* **360**, 751–758 (2018).
81. Lamark, T. & Johansen, T. Aggrephagy: selective disposal of protein aggregates by macroautophagy. *Int. J. Cell Biol.* **2012**, 736905–736921 (2012).
82. Deng, H., Dodson, M. W., Huang, H. & Guo, M. The Parkinson's disease genes pink1 and parkin promote mitochondrial fission and/or inhibit fusion in Drosophila. *Proc. Natl Acad. Sci. USA* **105**, 14503–14508 (2008).
83. Elliott, D. A. & Brand, A. H. The GAL4 system: a versatile system for the expression of genes. *Methods Mol. Biol. (Clifton, NJ)* **420**, 79–95 (2008).
84. Tang, Y., Tahmasebinia, F. & Wu, Z. Evaluation of mitochondrial function and morphology in drosophila. *Methods Mol. Biol. (Clifton, NJ)* **2322**, 195–206 (2021).
85. Bhattacharya, U., Neizer-Ashun, F., Mukherjee, P. & Bhattacharya, R. When the chains do not break: the role of USP10 in physiology and pathology. *Cell death Dis.* **11**, 1033 (2020).
86. Wang, X. et al. The deubiquitinase USP10 regulates KLF4 stability and suppresses lung tumorigenesis. *Cell death Differ.* **27**, 1747–1764 (2020).
87. Yuan, J., Luo, K., Zhang, L., Cheville, J. C. & Lou, Z. USP10 regulates p53 localization and stability by deubiquitinating p53. *Cell* **140**, 384–396 (2010).
88. Mila, M., Alvarez-Mora, M. I., Madrigal, I. & Rodriguez-Revenga, L. Fragile X syndrome: An overview and update of the FMR1 gene. *Clin. Genet.* **93**, 197–205 (2018).
89. Nally, J. E. et al. Pathogenic leptospires modulate protein expression and post-translational modifications in response to mammalian host signals. *Front. Cell. Infect. Microbiol.* **7**, 362 (2017).
90. Prasad, S. K., Singh, V. V., Acharjee, A. & Acharjee, P. Elucidating hippocampal proteome dynamics in moderate hepatic encephalopathy rats: insights from high-resolution mass spectrometry. *Exp. brain Res.* **242**, 1659–1679 (2024).
91. Zhang, Y. et al. Tumor editing suppresses innate and adaptive antitumor immunity and is reversed by inhibiting DNA methylation. *Nat. Immunol.* **25**, 1858–1870 (2024).
92. Subramanian, A. et al. Gene set enrichment analysis: a knowledge-based approach for interpreting genome-wide expression profiles. *Proc. Natl Acad. Sci. USA* **102**, 15545–15550 (2005).
93. Li, H. et al. Destabilization of TP53 by USP10 is essential for neonatal autophagy and survival. *Cell Rep.* **41**, 111435 (2022).
94. Geng, J. et al. ZNF598 responds to mitochondrial stress to abort stalled translation on mitochondrial outer membrane and maintain tissue homeostasis. *bioRxiv*, 2022.2002.2004.479092 (2022).
95. Geng, J. et al. Deregulation of ER-mitochondria contact formation and mitochondrial calcium homeostasis mediated by VDAC in fragile X syndrome. *Developmental cell* **58**, 597–615.e10 (2023).
96. Gomez-Suaga, P., Paillusson, S. & Miller, C. C. J. ER-mitochondria signaling regulates autophagy. *Autophagy* **13**, 1250–1251 (2017).
97. Honrath, B. et al. Glucose-regulated protein 75 determines ER-mitochondrial coupling and sensitivity to oxidative stress in neuronal cells. *Cell death Discov.* **3**, 17076 (2017).
98. Csordás, G., Weaver, D. & Hajnóczky, G. Endoplasmic reticulum-mitochondrial contactology: structure and signaling functions. *Trends cell Biol.* **28**, 523–540 (2018).
99. Yang, R. et al. Mitochondrial Ca^{2+} and membrane potential, an alternative pathway for Interleukin 6 to regulate CD4 cell effector function. *eLife* **4**, e06376 (2015).
100. Liang, J. R., Lingeman, E., Ahmed, S. & Corn, J. E. Atlastins remodel the endoplasmic reticulum for selective autophagy. *J. cell Biol.* **217**, 4049–4050 (2018).
101. Wang, R. et al. PINK1, Keap1, and Rtnl1 regulate selective clearance of endoplasmic reticulum during development. *Cell* **186**, 4172–4188.e18 (2023).
102. Wu, Z. et al. Tricornered/NDR kinase signaling mediates PINK1-directed mitochondrial quality control and tissue maintenance. *Genes Dev.* **27**, 157–162 (2013).
103. Liu, S. & Lu, B. Reduction of protein translation and activation of autophagy protect against PINK1 pathogenesis in Drosophila melanogaster. *PLoS Genet.* **6**, e1001237 (2010).
104. Saxton, R. A. & Sabatini, D. M. mTOR signaling in growth, metabolism, and disease. *Cell* **168**, 960–976 (2017).

105. Udagawa, T. et al. Failure to degrade CAT-Tailed proteins disrupts neuronal morphogenesis and cell survival. *Cell Rep.* **34**, 108599 (2021).
106. Dubnikov, T., Ben-Gedalya, T. & Cohen, E. Protein quality control in health and disease. *Cold Spring Harb. Perspect. Biol.* **9**, a023523 (2017).
107. Kampen, K. R., Sulima, S. O., Vereecke, S. & De Keersmaecker, K. Hallmarks of ribosomopathies. *Nucleic acids Res.* **48**, 1013–1028 (2020).
108. Yao, R. Q., Ren, C., Xia, Z. F. & Yao, Y. M. Organelle-specific autophagy in inflammatory diseases: a potential therapeutic target underlying the quality control of multiple organelles. *Autophagy* **17**, 385–401 (2021).
109. Cai, T. et al. The mitochondrial stress-induced protein carboxyl-terminal alanine and threonine tailing (msiCAT-tailing) promotes glioblastoma tumorigenesis by modulating mitochondrial functions. *eLife* **13**, https://doi.org/10.1101/2024.05.15.594447 (2024).
110. Laver, J. D. et al. The RNA-binding protein rasputin/g3bp enhances the stability and translation of its target mRNAs. *Cell Rep.* **30**, 3353–3367.e7 (2020).
111. Aguilera-Gomez, A., van Oorschot, M. M. & Veenendaa,l T., Rabouille C. In vivo vizualisation of mono-ADP-ribosylation by dPARP16 upon amino-acid starvation. *eLife* **5**, (2016).
112. Kedersha, N. L., Gupta, M., Li, W., Miller, I. & Anderson, P. RNA-binding proteins TIA-1 and TIAR link the phosphorylation of eIF-2 alpha to the assembly of mammalian stress granules. *J. cell Biol.* **147**, 1431–1442 (1999).
113. Reineke, L. C., Dougherty, J. D., Pierre, P. & Lloyd, R. E. Large G3BP-induced granules trigger eIF2α phosphorylation. *Mol. Biol. cell* **23**, 3499–3510 (2012).
114. Zhang, Y. J. et al. Poly(GR) impairs protein translation and stress granule dynamics in C9orf72-associated frontotemporal dementia and amyotrophic lateral sclerosis. *Nat. Med.* **24**, 1136–1142 (2018).
115. Lee, K. H. et al. C9orf72 dipeptide repeats impair the assembly, dynamics, and function of membrane-less organelles. *Cell* **167**, 774–788.e17 (2016).
116. Gasset-Rosa, F. et al. Cytoplasmic TDP-43 de-mixing independent of stress granules drives inhibition of nuclear import, loss of nuclear TDP-43, and cell death. *Neuron* **102**, 339–357.e7 (2019).
117. Jain, S. et al. ATPase-modulated stress granules contain a diverse proteome and substructure. *Cell* **164**, 487–498 (2016).
118. Wheeler, J. R., Jain, S., Khong, A. & Parker, R. Isolation of yeast and mammalian stress granule cores. *Methods (San. Diego, Calif.)* **126**, 12–17 (2017).
119. Antar, L. N., Afroz, R., Dictenberg, J. B., Carroll, R. C. & Bassell, G. J. Metabotropic glutamate receptor activation regulates fragile x mental retardation protein and FMR1 mRNA localization differentially in dendrites and at synapses. *J. Neurosci.: Off. J. Soc. Neurosci.* **24**, 2648–2655 (2004).
120. Repici, M. et al. The Parkinson's disease-linked protein DJ-1 associates with cytoplasmic mrnp granules during stress and neurodegeneration. *Mol. Neurobiol.* **56**, 61–77 (2019).
121. Shen, M. et al. Species-specific FMRP regulation of RACK1 is critical for prenatal cortical development. *Neuron* **111**, 3988–4005.e11 (2023).
122. Yang, Y. et al. Mitochondrial pathology and muscle and dopaminergic neuron degeneration caused by inactivation of Drosophila Pink1 is rescued by Parkin. *Proc. Natl Acad. Sci.* **103**, 10793–10798 (2006).
123. Xiao, G., Wan, Z., Fan, Q., Tang, X. & Zhou, B. The metal transporter ZIP13 supplies iron into the secretory pathway in Drosophila melanogaster. *Elife* **3**, 03191 (2014).
124. Motori, E. et al. Inflammation-induced alteration of astrocyte mitochondrial dynamics requires autophagy for mitochondrial network maintenance. *Cell Metab.* **18**, 844–859 (2013).
125. Gehrke, S. et al. PINK1 and Parkin control localized translation of respiratory chain component mRNAs on mitochondria outer membrane. *Cell Metab.* **21**, 95–108 (2015).
126. Lee, K. S. et al. Roles of PINK1, mTORC2, and mitochondria in preserving brain tumor-forming stem cells in a noncanonical notch signaling pathway. *Genes & Develop.* **27**, 2642–2647 (2013).
127. Dunn, K. W., Kamocka, M. M. & McDonald, J. H. A practical guide to evaluating colocalization in biological microscopy. *Am. J. Physiol. Cell Physiol.* **300**, C723–C742 (2011).
128. Huang, Y. et al. Pantothenate kinase 2 interacts with PINK1 to regulate mitochondrial quality control via acetyl-CoA metabolism. *Nat. Commun.* **13**, 2412 (2022).
129. Johnson, W. E., Li, C. & Rabinovic, A. Adjusting batch effects in microarray expression data using empirical Bayes methods. *Biostatistics (Oxf., Engl.)* **8**, 118–127 (2007).
130. Leek, J. T., Johnson, W. E., Parker, H. S., Jaffe, A. E. & Storey, J. D. The sva package for removing batch effects and other unwanted variation in high-throughput experiments. *Bioinforma. (Oxf., Engl.)* **28**, 882–883 (2012).
131. Ritchie, M. E. et al. limma powers differential expression analyses for RNA-sequencing and microarray studies. *Nucleic acids Res.* **43**, e47 (2015).
132. Wickham H. Data analysis. In: *ggplot2*). Springer (2016).
133. Croft, D. et al. Reactome: a database of reactions, pathways and biological processes. *Nucleic acids Res.* **39**, D691–D697 (2011).
134. Wu, Z. https://BioRender.com/l89m861 (2025).
135. Wu, Z. https://BioRender.com/u79p462 (2025).
136. Wu, Z. https://BioRender.com/f69z770 (2025).

Acknowledgements

We are grateful to Drs. Andrea Daga (Scientific Institute IRCCS E, Lecco, Italy), Leo Pallanck (University of Washington, Seattle, Washington), Jiahui Han (Xiamen University, Xiamen, Fujian, China), Alex Whitworth (University of Cambridge, London, UK), Xiaolin Bi (Dalian Medical University, Dalian, Liaoning, China), Nicholas Samuel Sokol (Indiana University Bloomington, Bloomington, Indiana), Elizabeth R. Gavis (Princeton University, Princeton, New Jersey), Bingwei Lu (Stanford University, Stanford, California) and Dario R Alessi (University for Dundee, Dundee, UK) for antibodies. We thank Drs. Richard Youle (National Institute of Neurological Disorders and Stroke, Bethesda, Maryland), and Yuzuru Imai (Juntendo University, Tokyo, Japan) for cell lines; and Drs. Nancy Kedersha (Harvard University, Boston), Paul Anderson (Harvard University, Boston), Toshifumi Inada (Tohoku University, Sendai, Japan), Bingwei Lu and Masahiro Fujii (Niigata University, Niigata, Japan) for plasmids. We are also grateful to Drs. William Saxton (Indiana University Bloomington, Bloomington, Indiana), Fumiko Kawasaki (RIKEN, Tokyo, Japan), Serge Birman (Paris Sciences et Lettres University, Paris, France), Shian Wu (NanKai University, Tianjin, China), Xiaolin Bi, Chun-Hong Chen (National Health Research Institutes, Taiwan), Dr. Patrik Verstreken (VIB-KU Leuven Center for Brain & Disease Research, Leuven, Belgium), Rongwei Xi (NIBS, Beijing, China), Tao Wang (National Institute of Biological Sciences, Beijing, China), Lmiguel Martins (Cell Death Regulation Laboratory, Leicester, UK.), Pankaj Kapahi (Buck Institute, Novato, California), Bingwei Lu, and the Vienna *Drosophila* RNAi Center, the FlyORF, and the Bloomington *Drosophila* Stock Center for *Drosophila* stocks. We thank the Snyder lab at Stanford University and the UT Southwestern Proteomics Core Facility for assistance with proteomics experiments. We thank Drs. Rebecca Jackson and Phoebe Doss at the UT Southwest EM Core Facility for assistance with TEM sample preparation and imaging. We also thank Dr. Hannes Vogel at Stanford University for discussing the TEM results. Special thanks go to all lab members of the Wu

lab at Southern Methodist University for discussions. This work was supported by the NIH (R15AG067470 and R35GM150190 to Z.W), the Cancer Prevention and Research Institute of Texas (RP210068 to Z.W), the Children's Brain Disease Foundation (to Z.W), the Scientific Innovation Program at ModeGene Inc. (U4174ZW202107 to Z.W). B. L is supported by the Ministry of Education, Singapore, under its Academic Research Fund Tier 2 (MOE-T2EP30123-0015) and Tier 1 (FY2023; 23-0434-A0001; 22-5800-A0001), the Precision Medicine Translational Research Programme Core Funding under NUHSRO/2020/080/MSC/04/PM, MGI IRP funding, NUS IT's Cloud Credits for Research Programme, and by the Singapore National Supercomputing Centre. Q.L was supported by the startup fund from Clemson University, and partially by the COBRE in Human Genetics (P20 GM139769 to Dr. Trudy F. C. Mackay and Dr. Robert R. H. Anholt) from the National Institute of General Medical Sciences.

Author contributions

F.T., Y.T., R.T. designed the study, performed the experiments, analyzed data, and co-wrote the manuscript. F.T., Y.T., R.T., Y.Z., W.B., M.O., B.L., S.C., R.J., L.J., Y.S., and Q.L. performed experiments and analyzed data. M.S. and B.L. provided resources for analyzing data. C.C. provided key reagents. B.L. & Z.W. conceived and supervised the study, performed experiments, wrote the manuscript, and provided funding.

Competing interests

The authors declare no competing interests.

Additional information

Supplementary information The online version contains supplementary material available at https://doi.org/10.1038/s41467-025-56346-3.

Correspondence and requests for materials should be addressed to Boxiang Liu or Zhihao Wu.

Peer review information *Nature Communications* thanks Haiteng Deng, Yuzuru Imai, and the other, anonymous, reviewer(s) for their contribution to the peer review of this work. A peer review file is available.

[1]Department of Biological Sciences, Dedman College of Humanities and Sciences, Southern Methodist University, Dallas, TX 75275, USA. [2]Department of Pharmacy and Pharmaceutical Sciences, Faculty of Science, National University of Singapore, Singapore 117543, Singapore. [3]Department of Genetics, Stanford University School of Medicine, Stanford, CA 94305, USA. [4]National Institute of Infectious Diseases and Vaccinology, NHRI, Miaoli 350401, Taiwan. [5]Department of Biological Sciences, Clemson University, Clemson, SC 29634, USA. [6]Center for Human Genetics, Clemson University, Greenwood, SC 29646, USA. [7]Department of Biomedical Informatics, Yong Loo Lin School of Medicine, National University of Singapore, Singapore 117543, Singapore. [8]Precision Medicine Translational Research Programme, Yong Loo Lin School of Medicine, National University of Singapore, Singapore, Singapore. [9]Cardiovascular-Metabolic Disease Translational Research Programme, Yong Loo Lin School of Medicine, National University of Singapore, Singapore 117543, Singapore. [10]NUS Centre for Cancer Research, Yong Loo Lin School of Medicine, National University of Singapore, Singapore 117543, Singapore. [11]Genome Institute of Singapore (GIS), Agency for Science, Technology and Research (A*STAR), 60 Biopolis Street, Singapore 138672, Singapore.
✉e-mail: boxiangliu@nus.edu.sg; zhihaowu@smu.edu